

## **Radar Backscatter across the Gulf Stream Sea Surface Temperature Front**

S. V. Nghiem<sup>1</sup>, F. K. Li<sup>1</sup>, E. J. Walsh<sup>2</sup>, and S. H. Lou<sup>1</sup>

<sup>1</sup>Jet Propulsion Laboratory  
California Institute of Technology  
Pasadena, California

<sup>2</sup>NASA Goddard Space Flight Center  
Observational Science Branch  
Laboratory for Hydrospheric Procesesses  
Wallops Flight Facility  
Wallops Island, Virginia

# Radar Backscatter across the Gulf Stream Sea Surface Temperature Front

S. V. Nghiem<sup>1</sup>, F. K. Li<sup>1</sup>, E. J. Walsh<sup>2</sup>, and S. H. Lou<sup>1</sup>

<sup>1</sup>Jet Propulsion Laboratory, MS 300-235

California Institute of Technology

4800 Oak Grove Drive

Pasadena, CA 91109

<sup>2</sup>NASA Goddard Space Flight Center

Observational Science Branch, Laboratory for Hydrospheric Processes

Wallops Flight Facility

Wallops Island, Virginia, USA

*Abstract* — Ocean backscatter signatures were measured by the Jet Propulsion Laboratory airborne NUSCAT K<sub>u</sub>-band scatterometer across the Gulf Stream sea surface temperature front. The measurements were made during the Surface Wave Dynamics Experiment (SWADE) off the coast of Virginia and Maryland in the winter of 1991. Vertical and horizontal backscatter data at multiple incidence angles were acquired in two different cases across the sea surface temperature boundary. Oceanic and atmospheric parameters were recorded in situ by buoys, direction wave spectra were measured by the Scanning Radar Altimeter (SRA) in addition to buoy wave spectral data, concurrent Advanced

---

<sup>2</sup> Presently on assignment at R/E/ET6, NOAA Environmental Technology Laboratory, Boulder, Colorado, USA.

Very High Resolution Radiometer (AVHRR) images were acquired, and Fleet Numerical Meteorology and Oceanography Center (FNMOC) analyzed surface current fields were obtained. For the vertical polarization, backscatter across the temperature front between the National Oceanic and Atmospheric Administration experimental coastal buoy (A) on the cold side and Discus-Central buoy (C) on the warm side shows a difference of more than 5 dB in several flight lines. Large frontal backscatter changes are observed in all upwind, downwind, and crosswind directions. The sea surface temperature difference measured by the buoys was about 9°C. The corresponding difference in wind speed cannot account for the large backscatter change in view of geophysical model functions depending only on neutral wind velocity such as SASS. For the case of horizontal polarization, backscatter changes are observed across the temperature front located between buoy C and Discus-East buoy (E). In this case, the FNMOC current field shows a ring at the center of the SWADE area, and buoy data report smaller wind speeds and a temperature difference approximately one half of that in the vertical backscatter case. On the cold side where the buoy wind speed was light ( $4.4\text{--}4.8 \text{ m} \cdot \text{s}^{-1}$ ), the maximum backscatter azimuth direction was not close to the upwind direction but located between the wind and the peak wave directions. For both vertical and horizontal polarization cases, NUSCAT data indicate that upwind backscatter on the cold side is smaller than or close to crosswind backscatter on the warm side for incidence angles larger than 20° and smaller than 60°. This suggests that the sea surface temperature front can be detected with backscatter data at these incidence angles for various wind directions over the cold and warm sides.

## I. INTRODUCTION

Sea surface temperature (SST) fronts affect the marine atmospheric boundary layer (MABL) and influence submesoscale processes in the coastal marine zone. Understanding effects of the temperature fronts has an important impact on coastal navigation, weather forecasting, climate study, and submesoscale to mesoscale ocean circulation. In a study of the effects of the SST front at the edge of the Gulf Stream on MABL, Wai and Stage [1] found that MABL was deeper over the warm water, a cloud layer associated with the mixed layer deepening formed over the warm ocean surface, and surface stress was much larger over the front and the warm side compared to the cold side. Jury [2] observed that the moist unstable MABL was 400 m deeper on the warm side and surface heat fluxes and wind stress increased as much as fivefold across the SST front on the northern edge of the Agulhas Current to the south of Africa. SST gradient across the Gulf Stream temperature front causes the strong baroclinicity of the MABL, which has a significant influence on the formation of cyclones and storms on the United States east coast [3] [4]. Xie and Lin [5] found that the elongated horizontal distribution of surface sensible heat fluxes along the Gulf Stream front is important to determine the effects on Carolina coastal frontogenesis. A mesovortex drifting toward the warm Gulf Stream water has an essential role in the initiation and organization of a new mesoscale convective system, which is associated with the genesis of intense vorticity in the boundary layer [6].

The Gulf Stream and the surface temperature front are quite dynamic. The stream path exhibits both wavelike spatial meanders due to instability processes and large-scale lateral shifts due to atmospheric forcing [7]. From data assimilation experiments in the

Gulf Stream regions, Ezer and Mellor [8] conclude that Gulf Stream position data are effective in nowcasting the deep Gulf Stream. The initialization and verification of Gulf Stream forecast model depend heavily on synoptic snapshots of the Gulf Stream north wall and ring locations [9]. The influx of warm Gulf Stream water oscillating in and out of the Carolina Bays is a process responsible for the onshore transport of fish larvae into coastal regions, and satellite observations of the stream is suggested to study variations in fish recruitment [10]. Genetically distinct populations of calanoid copepod are distributed in the western and eastern regions of the Gulf Stream [11]. The distributions of copepod species group are associated with physical properties across the Gulf Stream with separated group environments [12]. The fast moving Gulf Stream and its frontal eddies can cause adverse interactions of sea turtles with the fishery on the continental shelf near Cape Hatteras [13]. Oceanographic processes such as intrusions of Gulf Stream warm water as warm-core rings may trigger epizootics by infective agent transport or by environmental conditions promoting disease propagation [14]. In view of the above applications, monitoring the Gulf Stream SST front is important to severe weather forecast, marine resource management, and coastal environmental protection.

For radar remote sensing of the Gulf Stream SST front, variations of ocean backscatter associated with the changes in oceanic and atmospheric conditions need to be investigated. The advantage is that radar can see through cloud cover, which is quite frequent over the Gulf Stream region and persistent over 75% of the time [15] [16]. Over the past decades, a series of papers have been published to present results on radar backscatter across SST front. From measurements obtained during the Frontal Air-Sea Interaction Experiment (FASINEX) in 1986 over the Gulf Stream area, Li et al. [17] found an increase

as much as 2.5 dB in vertically polarized  $K_u$ -band backscatter at  $50^\circ$  incidence angle from the cold to warm side with a weak SST gradient of about  $2^\circ\text{C}$ . The backscatter change is attributed to the change in wind stress across the SST front [17]. Friehe et al. [18] showed large changes in wind stress corresponding to the SST frontal crossings in FASINEX. Askari et al. [19] observed that X-band real-aperture-radar cross-section variations at  $45^\circ$  incidence angle for horizontal polarization mostly depend on the local wind direction relative to the front and the change in wind stress across the front. These results, however, are based on an analysis using satellite AVHRR data and estimated wind speed and direction from the National Meteorological Center (NMC) due to the lack of ground truth [19]. From data taken during an experiment carried out in 1990 in the Gulf Stream region, Askari et al. [20] reported a change of 4.9 dB in  $K_u$ -band vertical backscatter at  $45^\circ$  incidence angle corresponding to a SST difference of  $6^\circ\text{C}$  and a wind speed about  $4\text{ m}\cdot\text{s}^{-1}$  for both cold and warm sides. In another case with  $4^\circ\text{C}$  SST change, the backscatter change was reduced to 3.6 dB for a wind speed of  $13.6\text{ m}\cdot\text{s}^{-1}$  assumed for both sides [20]. C-band scatterometer measurements in the vicinity of the Gulf Stream during the Surface Wave Dynamics Experiment (SWADE) indicated different behaviors in the anisotropy of ocean backscatter signature compared to classical or empirical model results [21]; however, the observations were limited to incidence angles less than  $21^\circ$  because the instrument was primarily designed to study directional wave spectra.

In this paper, we present  $K_u$ -band backscatter results, together with in situ oceanic and atmospheric measurements, SRA directional wave spectra, concurrent AVHRR SST imagery, and FNMOC surface current fields. Ocean backscatter signatures were acquired over Gulf Stream SST frontal crossings during the third intensive observation period (IOP)

of SWADE, conducted in the winter of 1991 (February-March). Both horizontal and vertical polarization backscatter data were taken with the Jet Propulsion Laboratory (JPL) airborne NUSCAT scatterometer at multiple incidence angles up to  $60^\circ$ . NUSCAT data at in full azimuth scans allow the SST frontal study in terms of backscatter azimuth modulation including effects on up, down, and crosswind radar cross-section ratios. In situ buoy data were obtained for both sides and directional wave spectra were also measured. Another difference from the above referenced work is that the SST gradient across the front was strong and the temperature difference reached up to  $9.0^\circ\text{C}$  in the vertical polarization case and  $4.6^\circ\text{C}$  in the horizontal polarization case. In view of  $K_u$ -band scatterometers such as QuickScat and SeaWinds to be launched by NASA to monitor global ocean conditions, the results of this SST front study on backscatter at  $K_u$  band are relevant for applications to the scatterometer data analyses.

## II. SURFACE WAVE DYNAMICS EXPERIMENT

The Surface Wave Dynamics Experiment was carried out in the winter of 1991 over an instrumented oceanic area off the coast of Virginia and Maryland. The scientific goals of SWADE are to understand the directional wave evolution and wave effects on momentum, heat, and mass fluxes at the ocean-atmosphere interface [22] [23]. In the third IOP of SWADE (February-March 1991), various airborne sensors [24], including the JPL NUSCAT  $K_u$ -band scatterometer, were flown over the experimental area to study the effect of wave field on the ocean backscatter response. We discuss here the experimental arrangement pertaining to the study of backscatter across the Gulf Stream SST front; further details of

the experiment have been reported by Caruso et al. [23] and Nghiem et al. [25].

The experimental area covered the north wall of the Gulf Stream where an array of buoys were deployed. The particular buoys used in this study include the National Oceanic and Atmospheric Administration (NOAA) experimental coastal buoy A (44024) located at  $37^{\circ}41.1'N$  and  $74^{\circ}42.9'W$ , discus buoy C (44023) at  $37^{\circ}32.1'N$  and  $74^{\circ}23.5'W$ , and discus buoy E (44015) at  $37^{\circ}29.0'N$  and  $73^{\circ}23.9'W$  (see Figure 3). Descriptions of the buoys and their data acquisitions have been presented elsewhere [26] [27] [24]. The buoys provide in situ oceanic and atmospheric data such as air and sea temperatures, wind speed and direction, stability parameter, atmospheric pressure, significant wave height, and directional wave spectrum for use in the backscatter study. Sea surface temperatures were also measured by the Precision Thermal Radiometer (PRT-5), an airborne nadir-viewing infrared radiometer system. In addition to wave data from buoys at fixed locations, directional wave spectra were obtained along various flight paths during SWADE with the Scanning Radar Altimeter (SRA), an airborne high resolution radar operating at 36 GHz [28].

During SWADE, NUSCAT was flown on the NASA Ames C-130 aircraft to measure ocean backscatter over a wide variety of oceanic and atmospheric conditions. NUSCAT is a dual-polarization scatterometer system operating at 14 GHz. NUSCAT has a high signal-to-noise ratio and a large dynamic range designed for airborne measurements of ocean backscatter for low to high wind conditions over a large range of incidence angles from flight altitudes up to 10000 m. The relative calibration accuracy for NUSCAT is estimated to be  $\pm 0.23$  dB and the absolute error is about  $\pm 1$  dB [25]. A special feature of NUSCAT is the full azimuth scanning capability which allows the study of azimuthal modulation



signatures in ocean backscatter for all upwind, downwind, and crosswind directions as the aircraft flew across the SST front. There were many NUSCAT flights over the Gulf Stream under various environmental conditions. From these flights, we eliminate cases with large significant wave height ( $> 3$  m), measured by buoys, to avoid complicated interactions with the associated swells. Large swells can disturb the marine boundary layer, increase drag coefficients [29], and influence ocean backscatter signatures [25].

### III. DATA COLLECTION

The JPL  $K_u$ -band backscatter data were collected in azimuth from  $0^\circ$  to  $360^\circ$  in  $10^\circ$  steps for incidence angle from  $0^\circ$  to  $60^\circ$  also in  $10^\circ$  steps. Figure 1 shows the NUSCAT antenna mounted at the tail of the C-130 aircraft (the antenna was covered inside a hemispherical radome during flight). The incidence and azimuth angles were controlled with a gimbal system seen as the base of the antenna in Figure 1. For each data run, the incidence angle and polarization were fixed and the azimuth angle was scanned once every 4 seconds for each of the  $10^\circ$  steps while the aircraft flew in straight a line across the Gulf Stream SST front. The advantage of this NUSCAT data collection procedure is that backscatter measurements can be obtained in full azimuth scans with more independent samples; however, horizontal and vertical polarizations were not operated simultaneously. From the SWADE data set, we select two sets of NUSCAT data runs: one for the vertical polarization data acquired on 28 February 1991 and the other for the horizontal polarization data on 9 March 1991. The backscatter data processing has been presented in recent publications by Nghiem et al. [25] [30].

Data from buoys were recorded in different types of records: one for wind vector, air and sea temperature, and other parameters; one for non-directional wave spectrum; and another for directional wave spectrum. All of these buoy data types are available except directional wave spectrum data at buoy A on the cold side in the case of vertical polarization backscatter. Buoy and NUSCAT data are coordinated by selecting backscatter measurements at the nearest location and the closest time relative to the buoys on the cold and warm sides of the Gulf Stream SST front. The average differences between buoy and NUSCAT measurements are 12 km in space and 17 minutes in time. In this analysis, we eliminate NUSCAT data obtained during transitional scans between cold and warm sides to avoid rapid changes in the data which were partly on the different sides of the SST front.

In addition to in-situ buoy data, SRA collected directional wave spectrum data over the SWADE area from the NASA Wallops P-3 aircraft. SRA scans a narrow beam across the ground track of the aircraft and measures the slant range to 64 points evenly spaced across the swath which are converted to surface elevations. Data over 5-6 km along track and 520 m cross-track are transformed into directional wave spectra by a two-dimensional fast Fourier transform. SRA data processing including Doppler correction and aircraft vertical motion removal have been presented elsewhere [28] [23]. SRA flight paths over the SWADE area are mapped in the report by Caruso et al. [23] during the period from 27 February to 7 March 1991, when SRA was in operation. SRA directional wave data are useful in complementary to buoy wave data especially when directional wave measurements are not available.

High-resolution infrared images of surface temperature were collected from AVHRR

on board the National Oceanic and Atmospheric Administration (NOAA) satellites NOAA-10, 11, and 12. Over the SWADE area, there were several ascending and descending passes per day primarily from NOAA-10, and the optimal daily coverage was typically in the early morning and late afternoon hours [23]. The AVHRR data were obtained and processed by the Remote Sensing Facility at Rosenstiel School of Marine and Atmospheric Science (RSMAS), University of Miami. We selected the AVHRR images with partial cloud cover where the Gulf Stream SST front was observable in SWADE buoy array area at the times closest to the two study cases.

Furthermore, analyzed surface current fields were derived from the FNMOC regional-scale circulation model DART (Data Assimilation Research and Transition). For the Gulf Stream region, this model uses two active layers and it is initialized with the dynamic height field from daily Gulf Stream temperature and salinity products [23]. FNMOC surface current data are given in terms of  $U$  and  $V$  components for every 6 hours starting at 00:00 hour. The data are specified on a spherical grid domain with a resolution of  $0.2^\circ$  in latitude and longitude. The field domain is limited to the Western North Atlantic and the Gulf Stream regions. Examples of AVHRR images and FNMOC current fields for SWADE are reported by Caruso et al. [23].

#### IV. GULF STREAM SEA SURFACE TEMPERATURE FRONT

By the end of 28 February and early 01 March 1991, the FNMOC surface current field at date 9103010000 (1991 March 01, 00:00 hour) in the left panel of Figure 2 indicates that the north wall of the Gulf Stream curved into the experimental area at the time of

NUSCAT vertical polarization measurements. This surface current condition had been persistent for several days. However, the current path quickly changed after a day as shown by the current field at date 9103020000 in the right panel of Figure 2, where the current flowed northeasterly and the current curl disappeared from the dense buoy array area. Note that the buoys are marked in red on the maps in Figure 2. The boundary of the sea surface temperature front is partially observed in the NOAA Advanced Very High Resolution Radiometer (AVHRR) image over the cloud-free region as presented in Figure 3, where the buoys were marks with triangles. Clouds, represented with the pink color in the image, were however covering a large area over the warm side. Buoy A was on the cold side and buoy C is on the warm side, and the SST difference measured by the buoys was around  $9^{\circ}\text{C}$ , which is in good agreement with the AVHRR SST. In a number of flights over the north wall of the Gulf Stream, NUSCAT crossed the sea surface temperature front and overpassed buoy A and buoy C. Frontal passages of the C-130 aircraft were verified with abrupt step changes in SST measurements by the downward looking PRT-5 (see the top panel of Figure 8).

A significant event during the third IOP of SWADE is the emergence of a warm-core ring at the center of the experimental area. This ring is seen just above the North wall of the Gulf Stream in the surface current field at date 9103100000 in the left panel of Figure 4 by the time of NUSCAT horizontal polarization flights. The ring had been existing at the same location since 7 March and it was still seen in the current field at 9103110000 in the right panel of Figure 4. During this period, the directional wave field became complicated with multi-modal sea states and steeper waves at shorter wavelengths caused by wave-current interactions [23]. Figure 5 presents the AVHRR sea surface temperature image

closest to the NUSCAT flight time. The image reveals part of the SST front with still some persistent clouds over the warm side. NUSCAT was flown between buoy C on the cold side and buoy E on the warm side. During these flights, the change in SST was about  $4^{\circ}\text{C}$  between buoys C and E across the SST front. The AVHRR image in Figure 5 shows the same amount of the temperature change between the buoy locations. The PRT-5 on the aircraft also observed the sharp change in SST (see the top panel in Figure 13). In the following sections, we present the ocean backscatter signatures corresponding to the above cases of the Gulf Stream and the associated SST conditions.

## V. VERTICAL BACKSCATTER ACROSS THE SST FRONT

### A. Physical Conditions

Oceanic and atmospheric conditions corresponding to the vertical polarization case are characterized by the parameters listed in Table 1. These parameters are taken directly from buoy measurements or derived from buoy data. The measured parameters include sea surface temperature  $T_{sea}$ , air temperature  $T_{air}$ , wind speed  $U(\text{buoy})$  at 5-m height for buoy A and at 4-m height for buoy C, wind direction  $\phi_{wind}$ , significant wave height  $H_{1/3}$ , wave direction  $\phi_{wave}$  of the spectral peak wave component, and dominant wave frequency  $f_0$ . For the National Data Buoy Center (NDBC) data, wind direction is defined as the direction from which the wind blows and wave direction is the direction from which the wave propagates. The derived parameters are stability parameter  $Z(10)/L$ , neutral wind speed  $U(19.5)$  at 19.5-m height, friction velocity  $u_*$ , and wave age  $c_0/u_*$ . The stability parameter is defined with roughness length  $Z(10)$  at 10-m height and Monin-Obukhov

length  $L$  [33]. The wave age is determined with phase speed  $c_0$  of the dominant gravity wave divided by friction velocity  $u_*$ . For each parameter, two numbers are given to present the variation of the parameter during the NUSCAT flight time between 23:00 and 24:00 GMT on 28 February 1991.

Sea surface temperature ( $T_{sea}$ ) measured by buoy A on the cold side was about 10.1°C and that at buoy C on the other side of the SST front was 19.1°C. The air temperature was only 1°C or less above the SST on the cold side. The warmer air gave a slightly stable condition as indicated by the positive values of the stability parameter  $Z(10)/L = 0.003$  to 0.082. The air temperature on the warm side was 4.2° – 4.7° lower than the SST and  $Z(10)/L$  showed unstable conditions with negative values between  $-0.125$  and  $-0.148$ . Under these conditions across the SST front, friction velocity increased by a factor of 1.7 from the cold to the warm side for the range of wind speeds in this case. The wind speeds were in the moderate range with neutral winds between 8.5-9.1 m·s<sup>-1</sup> and 13.5-14.0 m·s<sup>-1</sup> on the cold and warm sides, respectively. The wind directions were approximately from south-southwest at both buoys A and C and made small angles with respect to the proximate SST boundary. Significant wave height on the cold side was 1.5 time smaller than that on the warm side; note that this was about the same factor for the wind speed ratio of the two sides. Wave parameters  $\phi_{wave}$ ,  $f_0$ , and  $c_0/u_*$  were not available at buoy A for the present analysis. At buoy C, the wave direction was close to the wind direction with a dominant wave frequency at 0.2 Hz for a wave field at relatively small wave age  $c_0/u_* = 13.0$ .

## *B. Directional Wave Spectra*

NDBC 3-m discus buoys in the SWADE network were equipped with heave-pitch-roll sensors for directional wave spectrum measurements [31] [27]. Studies of wave spectra in the SWADE area have shown that wave-current interactions have a significant influence on wave propagation, energy, and directional spreading [32] [28]. For this present study, we use directional wave spectrum data from buoy C on the warm side of the Gulf Stream. Such data are not available from buoy A on the cold side and directional wave data obtained with SRA will be used.

Figure 6 presents wave spectra obtained from buoy C during the the NUSCAT vertical polarization data runs. The wave spectra are plotted in polar coordinates with the vertical axis pointed up to the north and the polar angle is in clockwise direction with  $90^\circ$  for east,  $180^\circ$  for south, and  $270^\circ$  for west. Wave directions at spectral peak (‘from-direction’ as defined in Section V.A above) are represented with white arrows whose radial lengths correspond to wave frequency in Hz. The yellow arrow denotes buoy-measured wind vector whose length is given in 50 times of the white radial scale. The orange vector, whose length is taken to be the same as the yellow one, shows the apparent wind direction determined by NUSCAT backscatter data; this will be discussed further in the next section. In the right panel of Figure 6, the NUSCAT wind vector, which coincides with the buoy wind vector, is plotted over the wind vector and thus only the orange arrow appears in this plot.

During the time of NUSCAT flights, the wave spectra shown in Figure 6 peaked at 0.19-0.20 Hz and the dominant waves became enhanced from 23:00 to 24:00 GMT while the wave direction rotated clockwise toward the west by just a few degrees. Figure 5 also

shows that the wind direction has a small rotation in the same direction. The direction changes are however within the measurement uncertainties and no definitive conclusion can be made. The longer wave component (at 0.1 Hz), propagating approximately from the east-northeast direction, was slightly diminishing. An examination of wave spectra at earlier times on the same date (28 February 1991) actually indicated that this longer wave component had been the dominant one [23].

SRA directional wave spectra are presented in Figure 7 for the cold side. The left panel is the wave spectrum at the time and location close to JPL NUSCAT radar data acquisition. This plot shows a dominant wave component at 0.1 Hz. This is a swell propagated from the east on the continent shelf toward the shore while the wind was blowing from the south-southwest as measured by buoy A. The right panel is another SRA directional wave spectrum located further westward (nearer to the shore) and taken at a later time. The latter spectrum shows some enhancement of the dominant wave and the wave direction was persistent toward the shore. Closer toward the shore, wave components propagated from southerly directions mostly vanished (see Walsh et al. [28] for further details of directional wave spectra). The corresponding significant wave heights given at the lower left corners of the plots also indicate higher waves nearer to the shore. Sea surface temperature measured at buoy A is also marked in the lower right corners of the plots. Comparing the buoy directional wave spectra on the warm side with the SRA spectra on the cold side shows that the swell system with  $f_0 = 0.1$  Hz came from the east-northeasterly direction and propagated across the SST front without much changing in wave directions.



### *C. Backscatter Results*

Figure 8 presents an example of ocean backscatter signature taken across the Gulf Stream SST front between buoys A and C under the wind and wave conditions discussed in the above sections. The top panel of Figure 8 plots SST measured by the PRT-5 on the C-130 aircraft. The SST boundary is clearly seen in the SST plot with the strong step change in temperature around 23:27 GMT (28 February 1991). The plot shows SST of 10.3°C and 17.4°C at locations near buoys A and C, respectively. The PRT-5 SST on the cold side is very close to the buoy SST of 10.1°C as given in Table 1. On the warm side, the SST measured from the aircraft was colder than that obtained from buoy data (19.1°C from Table 1). The difference could be caused by atmospheric effects in the path between the airborne PRT-5 radiometer and the sea surface on the warm side.

The upper middle panel of Figure 8 shows first-look backscatter data ( $\sigma_0$ ) in full azimuthal scan directions (360°) at incidence angles around 60° as NUSCAT flew across the SST front. The vertical polarization is denoted with VV in this plot. As observed from Figure 8, the backscatter manifests the step change across the SST front. Azimuth modulations in the backscatter signature are stronger with a large peak-to-peak value compared to the shallower azimuth modulation on the warm side. The incidence angle plot in Figure 8 indicates some small variations around the incidence angle commanded at 60°. This is due to a tilt in the antenna rotation axis caused by the difference between desired and operational pitch angles during NUSCAT flights. Effects of the incidence variations are accounted for in the NUSCAT data processor [30]. The bottom panel in Figure 8 shows the full azimuthal scanning capability of NUSCAT in terms of azimuth

angle with respect to north.

The apparent wind direction is defined as the azimuth angle at which the radar backscatter is maximum. Over a wind generated wave field, the apparent wind direction coincides with the actual wind direction because the sea surface roughness and slope are largest at upwind giving rise to the maximum backscatter. Apparent wind directions are determined directly from the NUSCAT data processor without relying either on geophysical model functions or on buoy measurements [30].

NUSCAT and buoy wind directions, plotted over the directional wave spectra in Figure 6 for the warm side and Figure 7 for the cold side, are close to or coincident with each other. In fact, the apparent wind directions retrieved from NUSCAT data from various flights vary between  $193^\circ$  and  $199^\circ$  compared to  $205^\circ$  measured by buoy A on the cold side, and between  $210^\circ - 217^\circ$  compared to  $214^\circ - 217^\circ$  by buoy C on the warm side of the Gulf Stream SST front. These observations suggest that the capillary waves primarily responsible for the backscatter signature are well aligned with the wind direction without much effects from large wave components for the corresponding wind speeds in the moderate range (see Table 1). These results on wind direction are consistent with a previous study of large wave effects on backscatter in the moderate wind range [25]. Furthermore, the significant wave height and wave age in Table 1 show that the large wave components are not very strong nor very well developed.

NUSCAT backscatter data at the vertical polarization for various SST crossings are processed to determine the corresponding backscatter values at upwind, crosswind, and downwind directions. SASS-II geophysical model function [34], which relates backscatter to neutral wind at 19.5-m height, is also used to calculate backscatter with wind speeds

and wind directions measured by buoys. The upper panels in Figure 9 compare vertical backscatter on both side of the SST front from  $20^\circ$  to  $60^\circ$  incidence angles for every  $10^\circ$  step at all of the up, cross, and downwind directions, except at  $40^\circ$  where data at downwind are not available. The plots show backscatter increases from the cold side to the warm side at all incidence angles.

At the small incidence of  $20^\circ$ , NUSCAT data agree well at all directions with model results accounting for the wind speed difference between the two sides. For the warm side where neutral wind speed  $U(19.5) = 13.5\text{--}14.0 \text{ m} \cdot \text{s}^{-1}$  under unstable conditions (see negative values of  $Z_0/L$  in Table 1 and the discussion in Section V.A), NUSCAT data at upwind and crosswind are slightly higher than model results at incidence angles larger than  $30^\circ$ . For the cold side where the wind speed range is lower under stable conditions with positive  $Z_0/L$  values, NUSCAT data are lower than model results at incidence angles between  $30^\circ$  and  $50^\circ$  for all of the directions.

The lower panels in Figure 9 compare backscatter changes between two sides of the Gulf Stream SST front. The backscatter change is defined as  $\Delta\sigma_{vv} = \sigma_{vv}(\text{warm side}) - \sigma_{vv}(\text{cold side})$  in the decibel (dB) domain. NUSCAT backscatter data show strong changes with differences of 4 dB to 7.5 dB in many cases. These changes are significantly higher than the model predictions for incidence angles from  $30^\circ$  to  $50^\circ$ . This is because NUSCAT data are lower than the calculated results on the stable cold side and higher on the unstable warm side. Backscatter changes are smaller at the small incidence angle of  $20^\circ$  and at the large incidence angle of  $60^\circ$ . In these cases, agreements on the backscatter changes between observed data and model calculations are better. Note that corresponding changes in wind speeds measured by buoys across the SST front is by a factor of 1.5 while changes

in friction velocities calculated from Large and Pond’s formulation [33] is by a larger factor of 1.7 because of air-sea temperature differences. However, actual measurements of friction velocity are not available at the times and locations of NUSCAT data acquisitions for the above cases.

Backscatter ratios are presented in Figure 10 for the cold side, the warm side, and the difference between the two sides. Here, the difference is defined as  $\text{ratio}(\text{warm side}) - \text{ratio}(\text{cold side})$  in the dB domain. The upper left and middle panels of Figure 10 show that NUSCAT ratios of upwind backscatter over downwind backscatter are larger than model results at incidence angles smaller than  $60^\circ$  for both sides. Thus, the upwind-downwind asymmetry is stronger in the observed data. The upper right panel indicates that differences in upwind-downwind backscatter ratios between the two sides are about 1 dB compared to model calculations, which are not very sensitive to incidence angle.

The lower left and middle panels in Figure 10 show that both NUSCAT and SASS-II ratios of upwind backscatter over crosswind backscatter are larger on the cold side compared to those on the warm side for incidence angles at  $40^\circ$  or larger. Thus the peak-to-peak azimuth modulations are stronger on the cold side, which have been observed in Figure 8 during the NUSCAT flight between buoys A and C. This trend is however reverse for incidence angles smaller than  $30^\circ$  where NUSCAT data have stronger azimuth modulations compared to the model results on both sides. Over the whole range of incidence angles, NUSCAT as well as SASS-II azimuth modulations become larger at larger incidence angles and the sensitivity is larger on the cold side. Unlike the upwind-downwind ratio changes, the upwind-crosswind ratio differences across the SST front seems to have a decreasing trend with larger incidence angles as observed in the lower right panel of Figure 10.

Upwind (maximum) backscatter on the cold side and crosswind (minimum) backscatter on the warm side are plotted in Figure 11. At incidence angles from  $30^\circ$  to  $50^\circ$ , NUSCAT data show that the maximum backscatter on the cold side is very close to or even a little smaller than the minimum backscatter on the warm side of the Gulf Stream. Model results are also plotted for comparisons. The observed data in Figure 11 suggest that backscatter at vertical polarization can be used to identify the cold side and the warm of the Gulf Stream in this case for most of the different wind directions on the two sides, except when the wind direction is turned by around  $90^\circ$  or almost perpendicular from one side to the other side.

## VI. HORIZONTAL BACKSCATTER ACROSS THE SST FRONT

### A. Physical Conditions

NUSCAT data runs for the horizontal polarization across the Gulf Stream SST front occurred on 9-10 March 1998. Table 2 summarizes corresponding oceanic and atmospheric conditions obtained from buoy C on the cold side and buoy E on the warm side. Two numbers are reported for each parameter to indicate the variation during NUSCAT measurements. Sea surface temperature ( $T_{sea}$ ) recorded by buoy on the cold side ranged from  $14.9^\circ\text{C}$  to  $16.0^\circ\text{C}$  and the temperature on the warm side was slightly above  $19^\circ\text{C}$ . Compared to the case of vertical polarization, air temperature ( $T_{air}$ ) was colder on both sides due to the passage of a cold front and  $T_{air}$  varied between  $4.8^\circ\text{C}$  to  $5.8^\circ$  on the cold side and between  $5.5^\circ\text{C}$  to  $7.1^\circ$  on the warm side. These resulted in unstable conditions with  $Z(10)/L = -2.08$  to  $-1.88$  for the cold side and less unstable conditions with

$Z(10)/L = -1.13$  to  $-0.82$  for the warm side. Wind speeds were in the light wind range to the moderate wind range from the cold to the warm side, respectively (see Table 2). Across the SST front, friction velocity  $u_*$  increased by more than 50% from  $4.4\text{--}4.6 \text{ m}\cdot\text{s}^{-1}$  to  $7.0\text{--}7.6 \text{ m}\cdot\text{s}^{-1}$ . The winds were from northerly directions due to the cold front, which interrupted the south and southwesterly wind pattern earlier in the third IOP of SWADE. The northerly wind directions made large angles with respect the general boundary of the SST front in the vicinity of buoys C and E. Significant wave heights were slightly smaller on the cold side with wave direction  $\phi_{wave}$  rotated clockwise to the east compared to that at buoy E on the warm area. With the same dominant wave frequency  $f_0 = 0.15 \text{ Hz}$  on both sides, the cold side had larger wave age  $c_0/u_* = 42.0$  to  $51.4$  compared to  $c_0/u_* = 18.1$  to  $37.6$  on the other side.

### *B. Directional Wave Spectra*

Directional wave spectrum data are available from the discus buoys on both sides of the SST boundary. Figure 12 plots directional wave spectra obtained from buoy C on the cold side (lower panels) and from buoy E on the warm side (upper panels) during NUSCAT flight time. The upper panels in Figure 12 shows that both winds and waves on the warm side were from northerly directions. At the later time, buoy wind (yellow arrows) and wave (white arrows) directions were very well aligned and the wave field became weaker with a lower significant wave height (see upper panels in Figure 12). In the upper left panel in Figure 12, NUSCAT apparent wind (orange arrow) direction coincides with buoy wind and it is plotted over the buoy wind direction.

On the cold side, the plots in the lower panels in Figure 12 also shows that the

wave field became weaker at the later time while the wave direction at spectral peak were persistent from north-northeast. In contrast to the case on the warm side, dominant wave directions on the cold side made large angles with buoy wind directions, which were around north-northwest (see lower panels of Figure 12). The north-northwesterly wind could not locally generated the north-northeasterly wave system, which was a swell propagating into the local area. The white arrows show a frequency of 0.15 Hz for the wave spectral peak component on both sides of the SST front. Significant wave heights and sea surface temperatures measured by the buoys are also given on the plots.

### *C. Backscatter Results*

An example of NUSCAT horizontal backscatter results across the Gulf Stream SST front are presented in Figure 13. The top panel traces sea surface temperature observed with the PRT-5 as NUSCAT flew from the cold side to the warm side. The sharp temperature gradient is clearly seen at 23:36 GMT (9 March 1991) on the temperature plot. The PRT-5 temperatures are slightly lower than those measured by buoys listed in Table 2. Horizontal (HH) backscatter data around  $60^\circ$  incidence angle are presented in the upper middle panel of Figure 13. The backscatter demonstrates the step change as the NUSCAT antenna scanned across the SST front. Note that harmonic azimuth modulations in ocean backscatter beat with incidence angle modulations causing complex azimuth patterns in the first-look backscatter data as plotted in Figure 13, Effects of incidence angle modulations are accounted for in the NUSCAT data processor (Nghiem et al., 1997). The bottom panel of Figure 13 plots corresponding azimuth angles in full scans from  $0^\circ$  to  $360^\circ$ .

NUSCAT data are used to determine apparent wind directions shown in Figure 12

(orange arrows). On the warm side, NUSCAT and buoy wind directions are either coincident or very close to each other. From several NUSCAT data runs on the warm side where the wind speed is in the moderate range, the apparent wind directions are from around  $12^\circ$  (a little to the right of north) and  $344^\circ$  (a little to the left of north) compared to  $3^\circ$  and  $344^\circ$  measured by buoy. For the cold side, the lower two panels in Figure 12 show that apparent wind directions (orange arrows) obtained from different NUSCAT data runs at different incidence angles are both close to the north ( $350^\circ$  and  $354^\circ$ ). Corresponding to these cases, buoy wind directions are close together and wave directions vary within a few degrees as seen in the buoy data (see the lower panels in Figure 12). Thus, NUSCAT apparent wind directions are in between buoy wind and wave directions. In fact, NUSCAT wind directions are  $29^\circ$ - $35^\circ$  to the right of the buoy wind directions and  $30^\circ$ - $35^\circ$  to the left of the wave directions. Note that the wind speed over the cold side is in the light wind range (see Table 2), which allows sea surface temperature [35] and swell [25] to have significant effects on radar backscatter. Comparing the two sides (vertical columns in Figures 12), the apparent wind directions perceived by NUSCAT are more continuous across the SST front while the buoy wind direction turns counterclockwise toward the west on the cold side and the wave direction rotates clockwise toward the east from the northerly direction on the warm side.

Upwind, downwind, and crosswind backscatter results from NUSCAT and SASS-II are compared in Figure 14 for incidence angles at  $20^\circ$ ,  $40^\circ$ , and  $60^\circ$  where backscatter data are obtained on both sides of the SST front. Both NUSCAT and SASS-II results show that backscatter increases from the cold side to the warm side. Similar to the case of the vertical polarization, experimental data and model calculations of the horizontal backscatter agree



well at  $20^\circ$  in terms of the absolute backscatter levels at upwind, downwind, and crosswind (upper panels in Figure 14), and in terms of backscatter change across the SST front (lower panels in Figure 14). At  $40^\circ$  incidence angle,  $\sigma_{hh}$  data compare very well with the model results on the warm side under moderate wind conditions while the data are consistently lower than the calculations at different azimuth directions giving rise to larger backscatter changes observed by NUSCAT across the front. These observed changes are large (around 5 dB or more) in all upwind, downwind, and crosswind directions. For  $60^\circ$  incidence angle,  $\sigma_{hh}$  data are mostly lower than model results while the observed backscatter increases (from cold to warm side) are lower at upwind and downwind and higher at crosswind as compared to the calculated backscatter changes.

Results for upwind-downwind and upwind-crosswind backscatter ratios are presented in Figure 15. Also similar to the vertical polarization case, the upwind-downwind backscatter ratio at  $20^\circ$  and  $40^\circ$  incidence angles for the horizontal polarization (upper left and middle panels in Figure 15) is larger for measured data. This indicates that NUSCAT observes a stronger upwind-downwind asymmetry. The upper right panel in Figure 15 show that SASS-II predicts virtually no change in the backscatter ratio between the two sides while NUSCAT data presents observable differences in the upwind-downwind ratio. The lower panels in Figure 15 indicates a stronger upwind-crosswind asymmetry in the measurements at  $20^\circ$  and  $40^\circ$ , where both NUSCAT and SASS-II suggest very little change in the upwind-crosswind ratio across the SST front. For  $60^\circ$  incidence angles, the backscatter ratio data and calculations do not compare well for both sides. Nevertheless, Figure 16 shows that the maximum backscatter at upwind on the cold side is close to or smaller (at  $40^\circ$ ) compared to the minimum backscatter at crosswind on the warm side, indicating

that horizontal backscatter can be used to identify the SST front, assuming an adequate resolution, for different wind directions on the two sides in this case.

## V. SUMMARY

We have presented  $K_u$ -band radar backscatter at incidence angles from  $20^\circ$  to  $60^\circ$  for vertical and horizontal polarizations measured by NUSCAT during SWADE across the Gulf Stream SST front. For the vertical polarization case, the SST gradient was as strong as  $9^\circ\text{C}$  across the front giving rise to a stable atmospheric boundary condition on the cold side and an unstable one on the warm sea surface which winds on the two sides were in the moderate range. A large increase is observed in the backscatter from the cold side to the warm side of the SST front while buoy data show higher wind speed on the warm side. The backscatter increase is underestimated by SASS-II model. Measured azimuth-modulation backscatter ratios are also different from the calculated values. These results indicate that the backscatter increase across the SST front is not simply dominant by the change in neutral wind speed. For the horizontal polarization case, a warm-core ring appeared on the north side of the Gulf Stream and the SST gradient was about  $4^\circ\text{C}$  under light winds on the cold side and moderate winds on the warm side. Similar to the vertical case, strong backscatter increase is observed across the SST boundary and measured backscatter signatures have stronger azimuth modulations compared to calculated values at  $40^\circ$  incidence angle. Furthermore, apparent wind directions seen by NUSCAT are between buoy wind and wave directions on the cold side where effects of swell can be important. In both cases, cold-side upwind backscatter is smaller or close to warm-side crosswind backscatter

for the middle range of incidence angles (30-50°), which suggests that the SST front can be detected by radar backscatter at these incidence angles for wind blowing in different directions over the cold and warm sides.

## ACKNOWLEDGMENT

The research described in this paper was carried out by the Jet Propulsion Laboratory, California Institute of Technology, under a contract with the National Aeronautics and Space Administration. The authors thank Dr. H. C. Graber of University of Miami for the AVHRR sea surface temperature data, FNMOC and Dr. R. E. Jensen of U.S. Army Corps of Engineers for the surface current fields, and Dr. J. D. Oberholtzer (retired from NASA Goddard Space Flight Center), Dr. K. E. Steele, and Dr. D. W. C. Wang of NOAA National Data Buoy Center for the buoy data.

## REFERENCES

- [1] M. M.-K. Wai and S. A. Stage, "Dynamical analyses of marine atmospheric boundary layer structure near the Gulf Stream oceanic front," *Q. J. R. Meteorol. Soc.*, Vol. 115, pp. 29-44, 1989.
- [2] M. R. Jury, "A thermal front within the marine atmospheric boundary layer over the Agulhas current south of Africa: composite aircraft observations," *J. Geophys. Res.*, vol. 99, no. C2, pp. 3297-3304, 1993.
- [3] C. Y. Huang and S. Raman, "Numerical simulation of January 28 cold air outbreak during GALE," *Boundary Layer Meteorol.*, vol. 56, pp. 51-81, 1991.
- [4] J. J. Cione, S. Raman, and L. J. Pietrafesa, "The effect of Gulf-Stream induced baroclinicity on U.S. east coast winter cyclones," *Mon. Weath. Rev.*, Vol. 121, pp. 421-430, 1993.
- [5] L. Xie and Y. L. Lin, "A numerical study of stratified air-flow over mesoscale heat-sources with application to Carolina coastal frontogenesis," *Monthly Weather Rev.*, vol. 124, no. 12, pp. 2807-2827, 1996.
- [6] D. L. Zhang and N. Bao, "Oceanic cyclogenesis as induced by a mesoscale convective system moving offshore. 2. Genesis and thermodynamic transformation," *Monthly Weather Rev.*, vol. 124, no. 10, pp. 2206-2225, 1996.
- [7] T. Lee and P. Cornillon, "Temporal variation of meandering intensity and domain-wide lateral oscillations of the Gulf-Stream," *J. Geophys. Res.*, vol. 100, no. C7, pp. 13603-13613, 1995.
- [8] T. Ezer and G. L. Mellor, "Data assimilation experiments in the Gulf-Stream region

- How useful are satellite-derived surface data for nowcasting the subsurface fields," *J. Atmos. Oceanic Tech.*, vol. 14, no. 6, pp. 1379-1391, 1997.
- [9] S. M. Glenn and M. F. Crowley, "Gulf-Stream and ring feature analyses for forecast model validation," *J. Atmos. Oceanic Tech.*, vol. 14, no. 6, pp. 1366-1378, 1997.
- [10] P. M. Stegmann and J. A. Yoder, "Variability of sea-surface temperature in the South-Atlantic bight as observed from satellite - Implications for offshore-spawning fish," *Continental Shelf Res.*, vol. 16, no. 7, pp. 843-, 1996.
- [11] A. Bucklin, T. C. Lajeunesse, E. Curry, J. Wallinga, and K. Garrison, "Molecular diversity of the copepod, *nannocalanus minor* - Genetic-evidence of species and population-structure in the North-Atlantic Ocean," *J. Marine Res.*, v54 (2), pp. 285-310, 1996.
- [12] C. J. Ashjian and K. F. Wishner, "Temporal persistence of copepod species groups in the Gulf-Stream," *Deep Sea Res., Part I, Oceanographic Research Papers*, vol. 40, no. 3, pp. 483-, 1993.
- [13] S. P. Epperly, J. Braun, A. J. Chester, F. A. Cross, J. V. Merriner, and P. A. Tester, "Winter distribution of sea-turtles in the vicinity of Cape-Hatteras and their interactions with the summer flounder trawl fishery," *Bull. Marine Sci.*, vol. 56, no. 2, pp. 547-568, 1995.
- [14] R. E. Scheibling and A. W. Hennigar, "Recurrent outbreak of disease in sea-urchins, *strongylocentrotus-droebachiensis*, in Nove-Scotia - Evidence for a link with large-scale meteorological and oceanographic events," *Marine Ecology Prog. Ser.*, vol. 152, pp. 155-165, 1997.
- [15] R. J. Alliss and S. Raman, "Cloudiness and its relationship to saturation pressure differences during a developing east-coast winter storm," *J. Appl. Meteor.*, vol. 34,

- no. 11, pp. 2367-2387, 1995a.
- [16] R. J. Alliss and S. Raman, "Quantitative estimates of cloudiness over the Gulf-Stream locale using GOES VAS observations," *J. Appl. Meteor.*, vol. 34, no. 2, pp. 500-510, 1995b.
- [17] F. Li, W. Large, W. Shaw, E. J. Walsh, and K. Davidson, "Ocean radar backscatter relationship with near-surface winds: A case study during FASINEX," *J. Phys. Oceanogr.*, vol. 19, no. 3, pp. 342-353, 1989.
- [18] C. A. Friehe, W. J. Shaw, D. P. Rogers, K. L. Davidson, W. G. Large, S. A. Stage, G. H. Crescenti, S. J. S. Khalsa, G. K. Greenhut, and F. Li, "Air-Sea Fluxes and Surface Layer Turbulence Around a Sea Surface Temperature Front," *J. Geophys. Res.*, vol. 96, no. C5, pp. 8593-8609, 1991.
- [19] F. Askari, G. L. Geernaert, W. C. Keller, and S. Raman, "Radar imaging of thermal fronts," *Int. J. Remote Sens.*, vol. 14, no. 2, pp. 275-294, 1993.
- [20] F. Askari, T. Donato, and W. C. Keller, "Airborne scatterometer detection of winds and sea surface roughness changes across the Gulf Stream front," *Remote Sens. Environ.*, vol. 53, pp. 31-45, 1995.
- [21] D. Hauser, G. Caudal, and L. K. Shay, "Behavior of the ocean radar cross-section at low incidence, observed in the vicinity of the Gulf-Stream," *IEEE Trans. Geosci. Remote Sens.*, vol. 33, no. 1, pp. 162-171, 1995.
- [22] R. A. Weller, M. A. Donelan, M. G. Briscoe, and N. E. Huang, "Riding the crest: A tale of two wave experiments," *Bull. Amer. Met. Soc.*, vol. 72, no. 2, pp. 163-183, 1991.
- [23] M. J. Caruso, H. C. Graber, R. E. Jensen, and M. A. Donelan, *Observations and Mod-*

- elling of Winds and Waves During the Surface Wave Dynamics Experiment; Report 2, Intensive Observation Period IOP-3, 25 February-9 March 1991*, Tech. Rep. CERC-93-6, US Army Corps of Engineers, Waterways Experiment Station, Washington, DC, March 1994.
- [24] D. Oberholtzer and M. Donelan, *SWADE Data Guide*, NASA Ref. Pub. 1388, National Aeronautic and Space Administration, Goddard Space Flight Center, Greenbelt, Maryland, 1996.
- [25] S. V. Nghiem, F. K. Li, S. H. Lou, G. Neumann, R. E. McIntosh, S. C. Carson, J. R. Carswell, E. J. Walsh, M. A. Donelan, and W. M. Drennan, "Observations of ocean radar backscatter at  $K_u$  and C bands in the presence of large waves during the Surface Wave Dynamics Experiment," *IEEE Trans. Geosci. Remote Sens.*, vol. 33, no. 3, pp. 708-721, 1995.
- [26] K. E. Steele, C.-C. Teng, and D. W. C. Wang, "Wave direction measurements using pitch-roll buoys," *Ocean Engng.*, vol. 19, no. 4, pp. 349-375, 1992.
- [27] F. C. Jackson and R. E. Jensen, "Wave-field response to frontal passages during SWADE," *J. Coastal Res.*, vol. 11, no. 1, pp. 34-67, 1995.
- [28] E. J. Walsh, L. K. Shay, H. C. Graber, A. Guillaume, D. Vandermark, D. E. Hines, R. N. Swift, and J. F. Scott, "Observations of surface wave-current interaction during SWADE," *Global Atmos. Ocean Sys.*, vol. 5, pp. 99-124, 1996.
- [29] M. A. Donelan, W. M. Drennan, and K. B. Katsaros, "The air-sea momentum flux in conditions of wind sea and swell," *J. Phys. Oceanogr.*, vol. 27, no. 10, pp. 2087-2099, 1997.
- [30] S. V. Nghiem, F. K. Li, and G. Neumann, "The dependence of ocean backscatter

- at K<sub>u</sub>-band on oceanic and atmospheric parameters,” *IEEE Trans. Geosci. Remote Sens.*, vol. 35, no. 3, pp. 581-600, 1997.
- [31] F. Anctil, M. A. Donelan, G. Z. Forristall, K. E. Steele, and Y. Ouellet, “Deep-water field-evaluation of the NDBC-SWADE 3-m discus directional buoy,” *J. Atmos. Oceanic Tech.*, vol. 10, no. 1, pp. 97-112, 1993.
- [32] D. W. Wang, A. K. Liu, C. Y. Peng, and E. A. Meindl, “Wave-current interaction near the Gulf Stream during the Surface Wave Dynamics Experiment,” *J. Geophys. Res.*, vol. 99., no. C3, pp. 5065-5079, 1994.
- [33] W. G. Large and S. Pond, “Open ocean momentum flux measurements in moderate to strong wind,” *J. Phys. Oceanogr.*, vol. 11, 324-336, 1981.
- [34] F. J. Wentz, S. Peteherych, and L. A. Thomas, “A model function for ocean radar cross sections at 14.6 GHz,” *J. Geophys. Res.*, Vol. 89, No. C3, pp. 3689-3704, 1984.
- [35] M. A. Donelan and W. J. Pierson, “Radar scattering and equilibrium ranges in wind-generated waves with application to scatterometry,” *J. Geophys. Res.*, vol. 92, no. C5, pp. 4971-5029, 1987.



## LIST OF FIGURES

- Figure 1** NUSCAT antenna and the gimbal system mounted under the tail of the NASA Ames C-130 aircraft. The photograph was taken with the radome removed.
- Figure 2** Fleet Numerical Meteorology and Oceanography Center (FNMOC) current fields: (a) the left panel is the FNMOC current field at the beginning of 1 March 1991, and (b) the right panel is the FNMOC current field 1 day later. Current directions are denoted with the arrows and current strengths are color coded.
- Figure 3** National Oceanic and Atmospheric Administration (NOAA) Advanced Very High Resolution Radiometer (AVHRR) image of sea surface temperature over the SWADE area on 1 March 1991. Part of the Gulf Stream sea surface temperature front is seen in the cloud-free area of the image. Cloud cover is assigned to 0°C represented with the dark pink color.
- Figure 4** Fleet Numerical Meteorology and Oceanography Center (FNMOC) current fields: (a) The left panel is the FNMOC current field at the beginning of 10 March 1991, and (b) the right panel is the FNMOC current field 1 day later. Current directions are denoted with the arrows and current strengths are color coded.
- Figure 5** National Oceanic and Atmospheric Administration (NOAA) Advanced Very High Resolution Radiometer (AVHRR) image of sea surface temperature over the SWADE area on 9 March 1991. Part of the Gulf Stream sea surface temperature front is seen in the cloud-free area of the image. Cloud cover is

assigned to 0°C represented with the dark pink color.

**Figure 6** Directional wave spectra in the frequency domain measured by buoy C on 28 February 1991: (a) the left panel is for 23:00 GMT, and (b) the right panel is the spectrum 1 hour later. The concentric dotted circles are at 0.1 Hz intervals and the radial dotted lines are 30° apart. The white arrow is for wave direction, yellow for wind vector measured by buoy, and orange for apparent wind direction obtained from NUSCAT data. For each plot, sea surface temperature is given at the lower right-hand corner and significant wave height at the left-hand corner.

**Figure 7** Directional wave spectra in the frequency domain measured by SRA on 28 February 1991: (a) the left panel is for 23:03:31 GMT at 37°14.8'N and 75°08.7'W, and (b) the right panel is for 23:05:41 GMT at 37°15.3'N and 75°18.6'W.

**Figure 8** NUSCAT data acquired on 2 February 1991: (a) the top panel is for surface temperature measured by the Precision Thermal Radiometer (PRT-5), (b) the upper middle panel shows NUSCAT backscatter at vertical polarization, (c) the lower middle panel is for incidence angle, and (d) the bottom panel is for azimuth angles.

**Figure 9** Backscatter at vertical polarization on the cold side and the warm side of the Gulf Stream sea surface temperature front: the top panels from left to right are for backscatter at upwind, downwind, and crosswind directions, and the lower panels are for corresponding backscatter changes between the two sides.

**Figure 10** Backscatter ratios at vertical polarization: the top panels from left to right

are for upwind-downwind ratios on the cold side, warm side, and differences between the two sides, and the lower panels are for upwind-crosswind ratios.

**Figure 11** Comparisons of upwind backscatter vertical polarization on the cold side with crosswind backscatter on the warm side. Both NUSCAT observations and SASS-II calculations are plotted.

**Figure 12** Directional wave spectra in the frequency domain measured by buoys E and C: (a) the upper left panel is for buoy E at 22:00 GMT on 9 March 1991, (b) the upper right panel is for buoy E at 02:00 GMT on 10 March 1991, (c) the lower left panel is for buoy C at 23:00 GMT on 9 March 1991, and (d) the lower right panel is for buoy C at 02:00 GMT on 10 March 1991. These plots arranged by the cold side in the bottom and the warm side on top; time increases from left to right. The concentric dotted circles are at 0.1 Hz intervals and the radial dotted lines are 30° apart. The white arrow is for wave direction, yellow for wind vector measured by buoy, and orange for apparent wind direction obtained from NUSCAT data. Sea surface temperature in °C and significant wave height in meter are given for each plot.

**Figure 13** NUSCAT data acquired on 9 March 1991: (a) the top panel is for surface temperature measured by the Precision Thermal Radiometer (PRT-5), (b) the upper middle panel shows NUSCAT backscatter at horizontal polarization, (c) the lower middle panel is for incidence angle, and (d) the bottom panel is for azimuth angles.

**Figure 14** Backscatter at horizontal polarization on the cold side and the warm side of the Gulf Stream sea surface temperature front: the top panels from left to

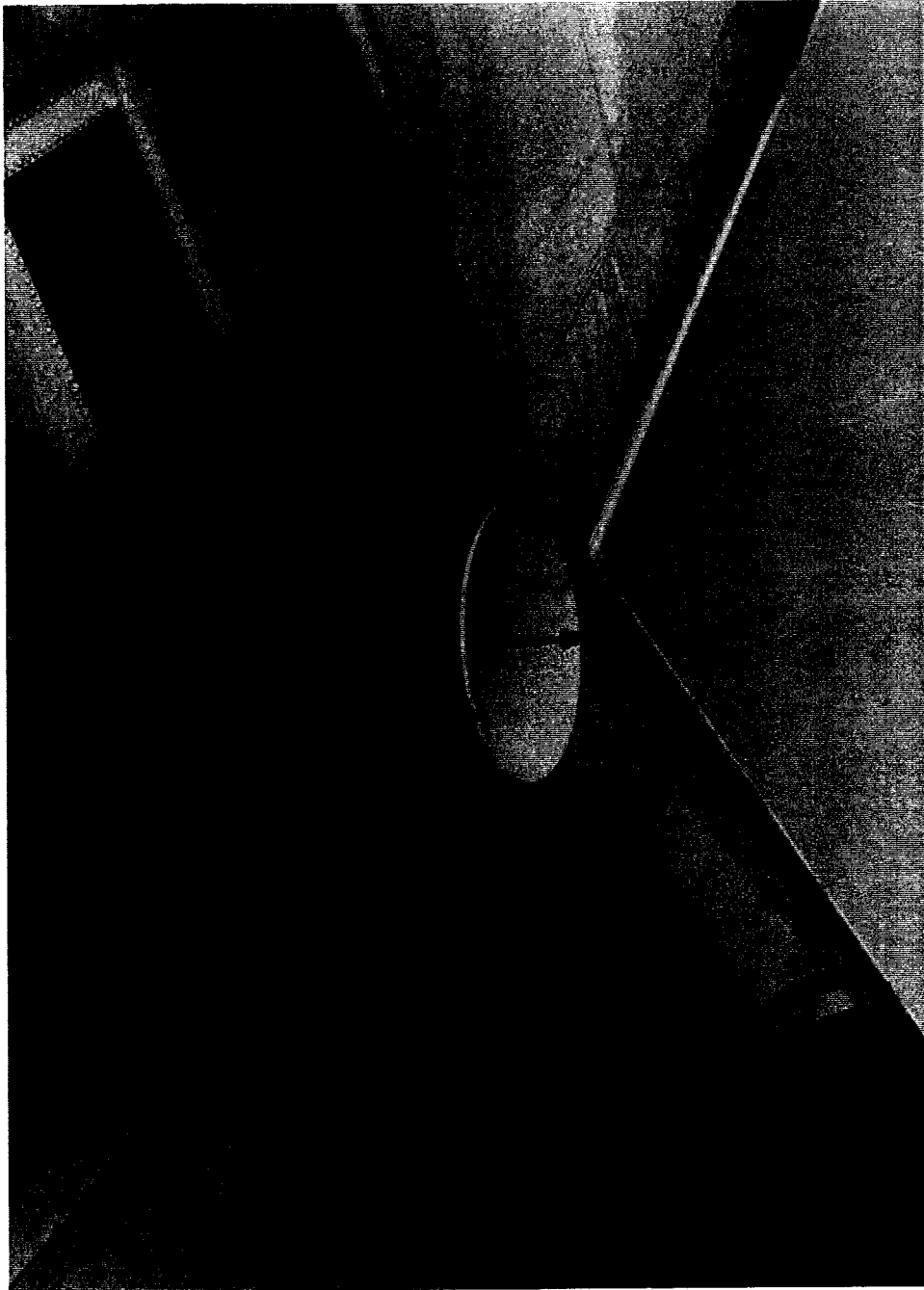
right are for backscatter at upwind, downwind, and crosswind directions, and the lower panels are for corresponding backscatter changes between the two sides.

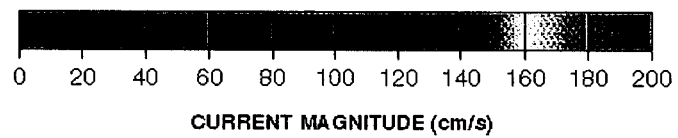
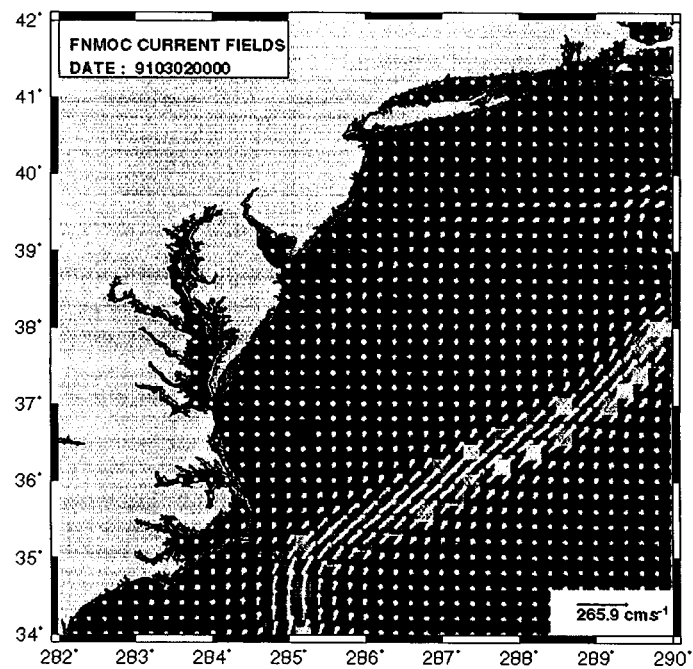
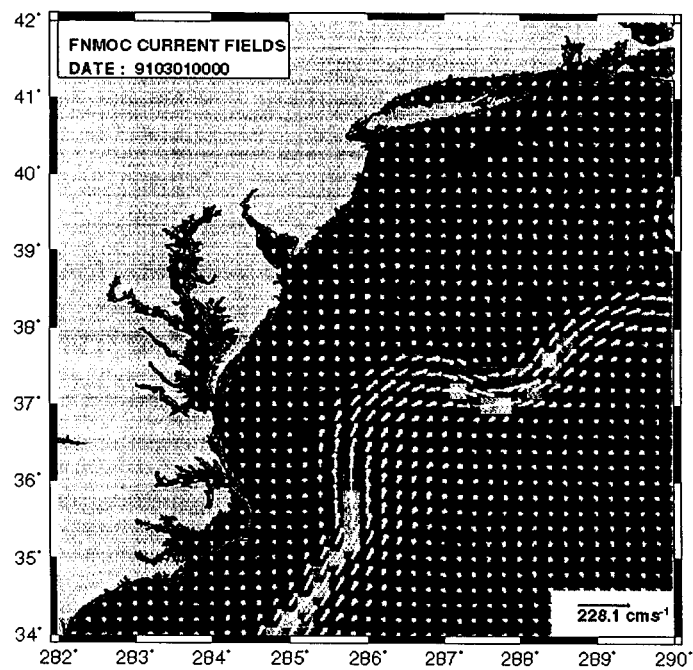
**Figure 15** Backscatter ratios at horizontal polarization: the top panels from left to right are for upwind-downwind ratios on the cold side, warm side, and differences between the two sides, and the lower panels are for upwind-crosswind ratios.

**Figure 16** Comparisons of upwind backscatter at horizontal polarization on the cold side with crosswind backscatter on the warm side. Both NUSCAT observations and SASS-II calculations are plotted.

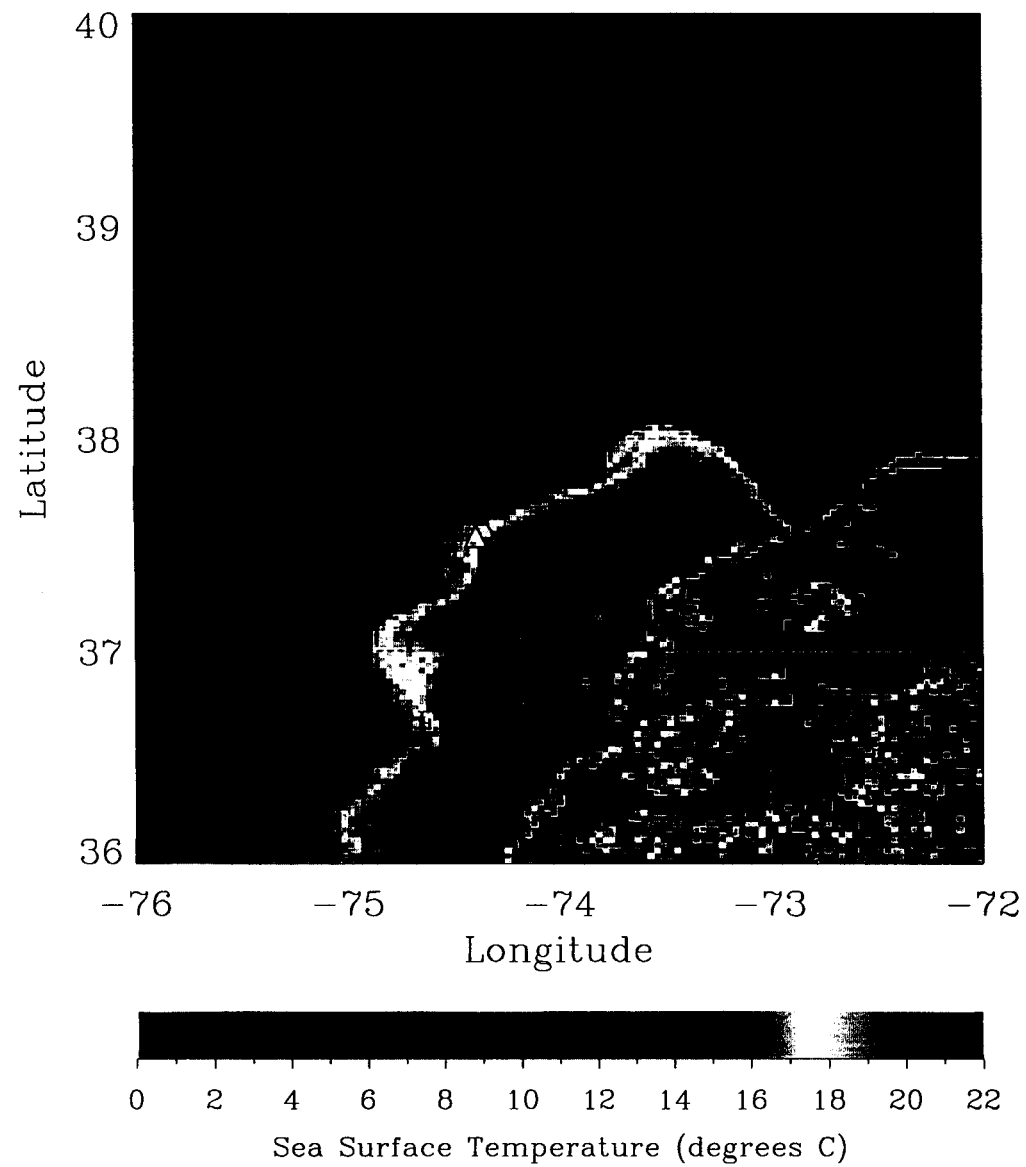
## LIST OF TABLES

- Table 1** Oceanic and atmospheric parameters measured by buoy or derived from buoy data for the case of NUSCAT vertical polarization. Buoy A data are used for the cold side and buoy C for the warm side.
- Table 2** Oceanic and atmospheric parameters measured by buoy or derived from buoy data for the case of NUSCAT horizontal polarization. Buoy C data are used for the cold side and buoy E for the warm side.

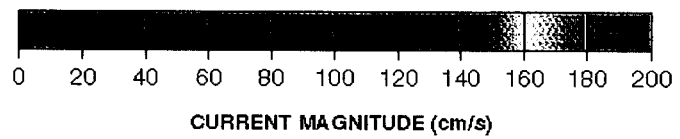
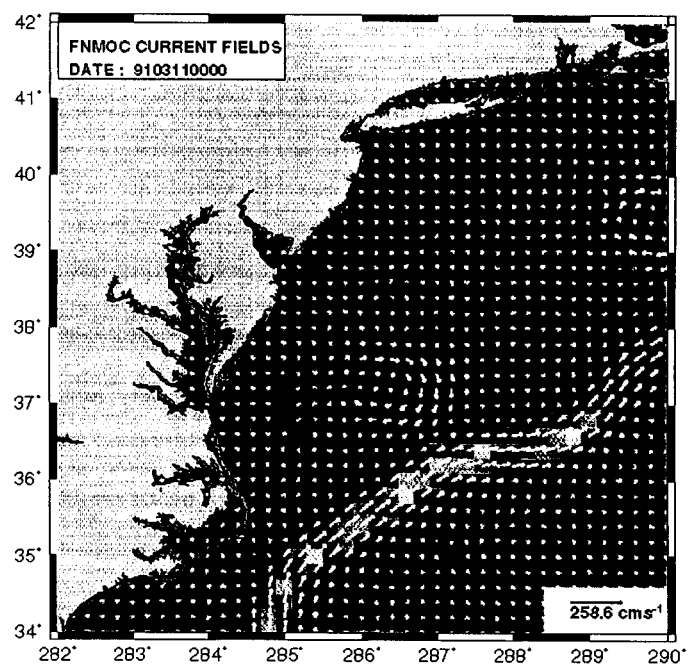
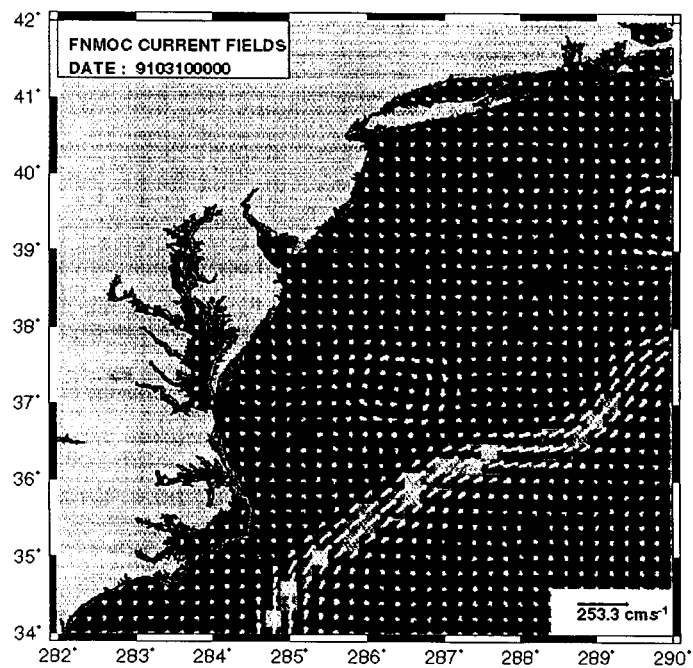




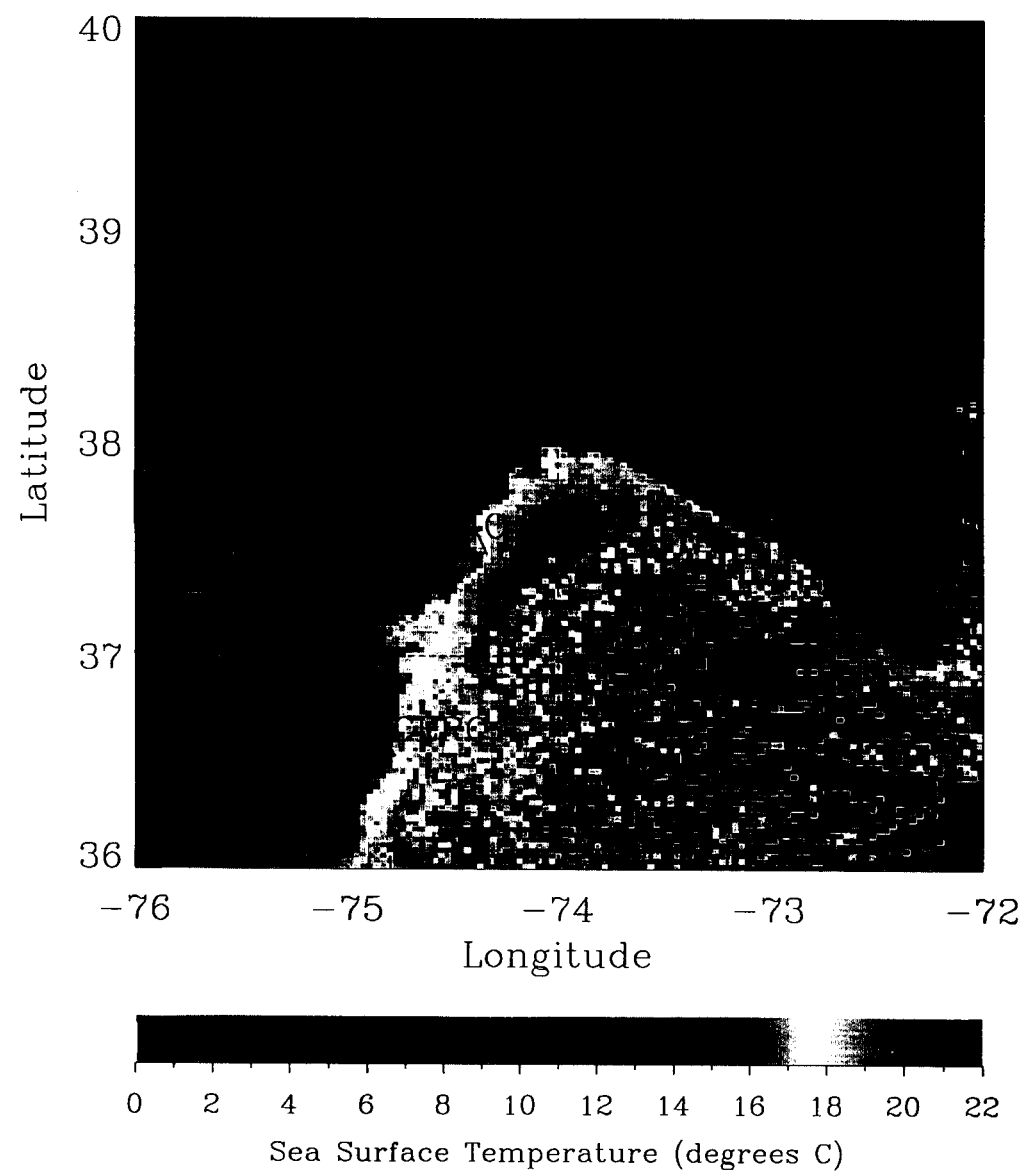
March 1, 1991; 07:34 (UTC)



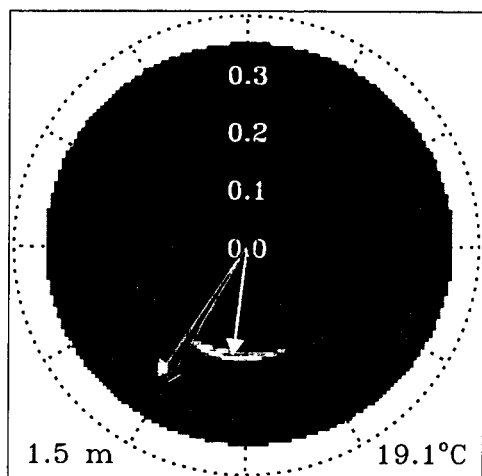




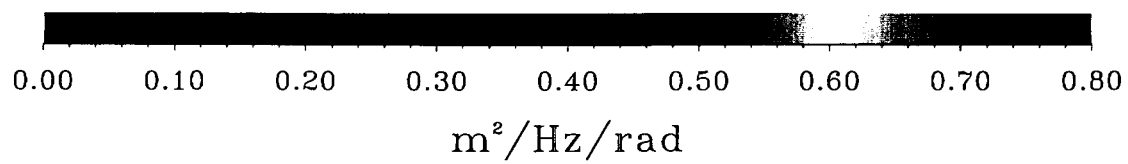
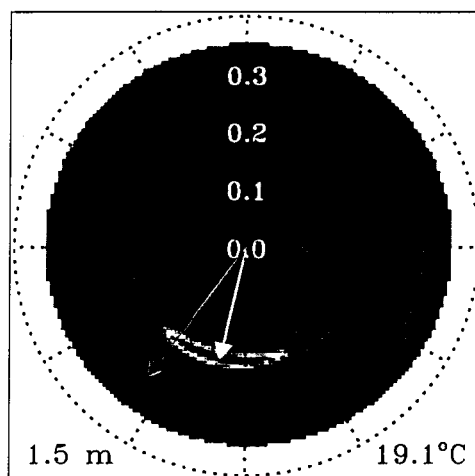
March 9, 1991; 19:12 (UTC)



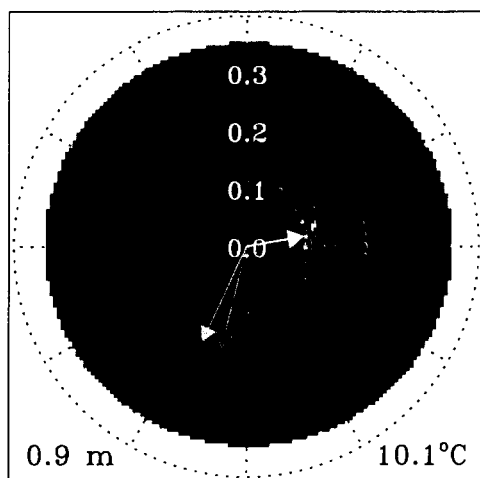
Buoy C: 91-02-28 23:00



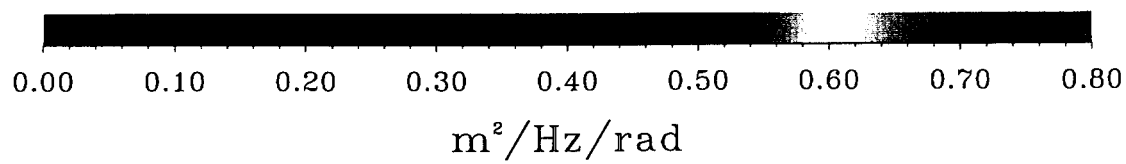
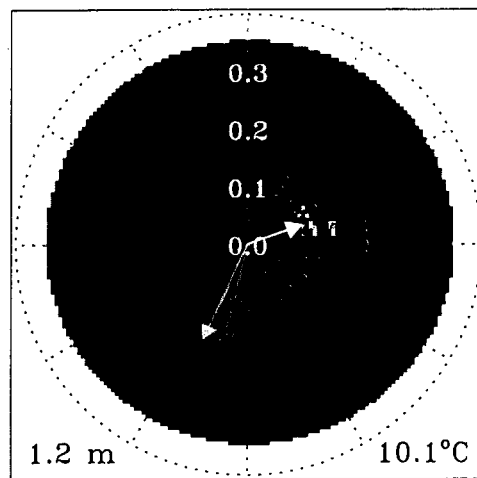
Buoy C: 91-02-28 24:00

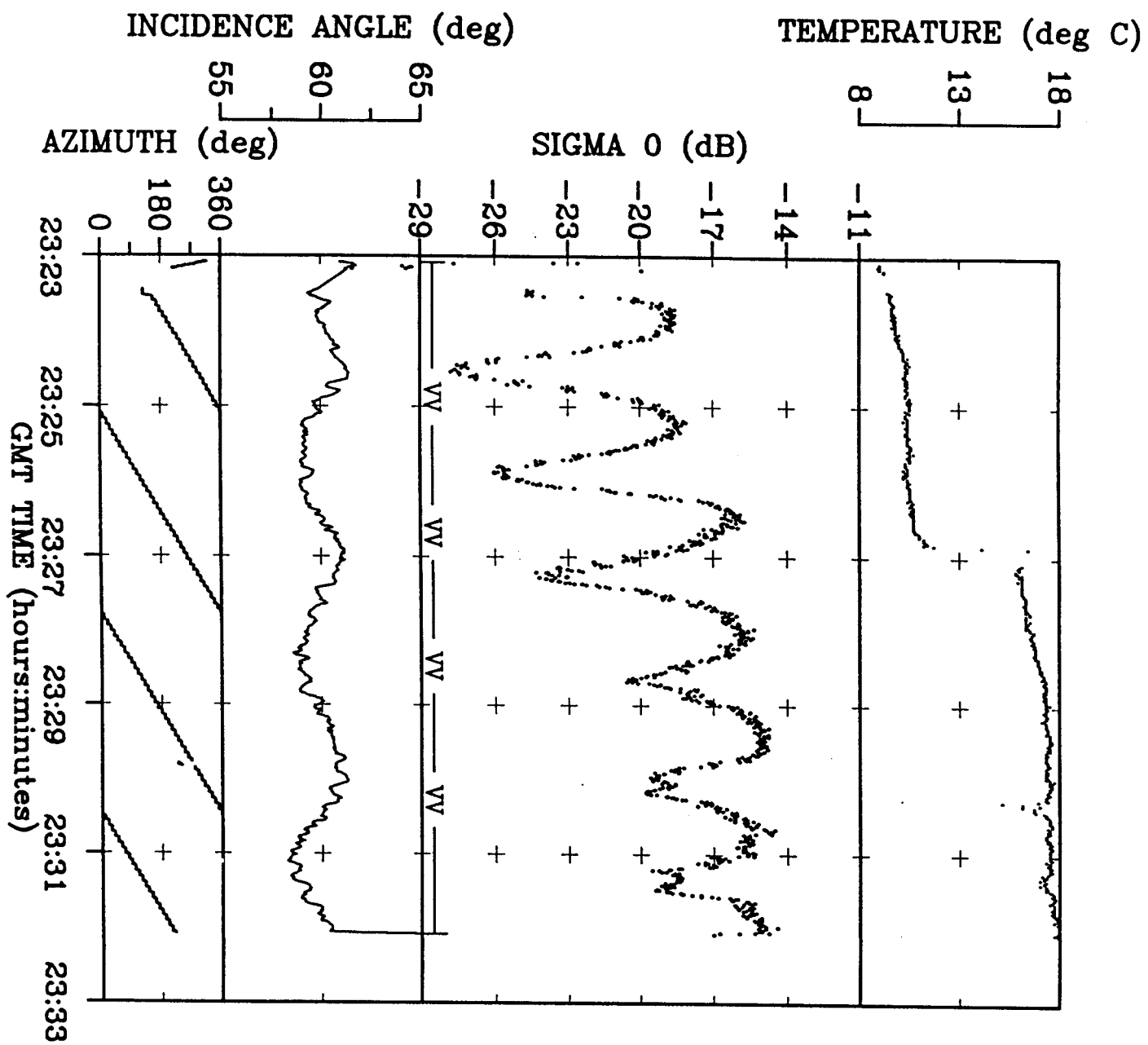


SRA: 91-02-28 23:03:31

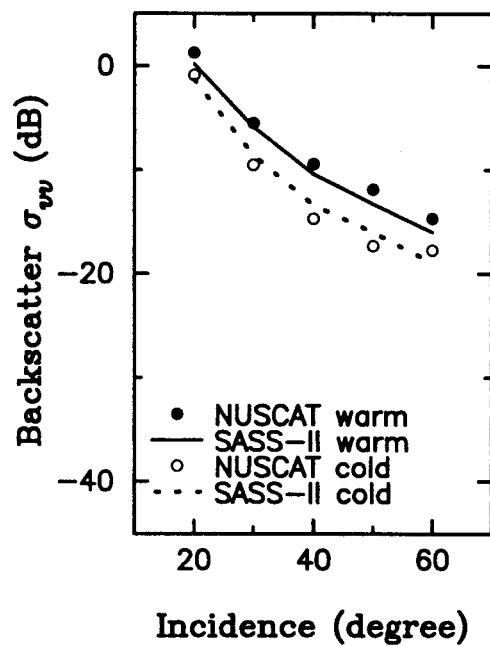


SRA: 91-02-28 23:05:41

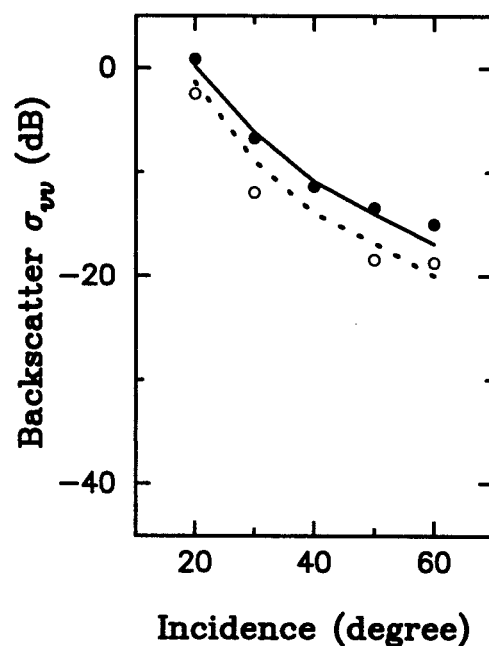




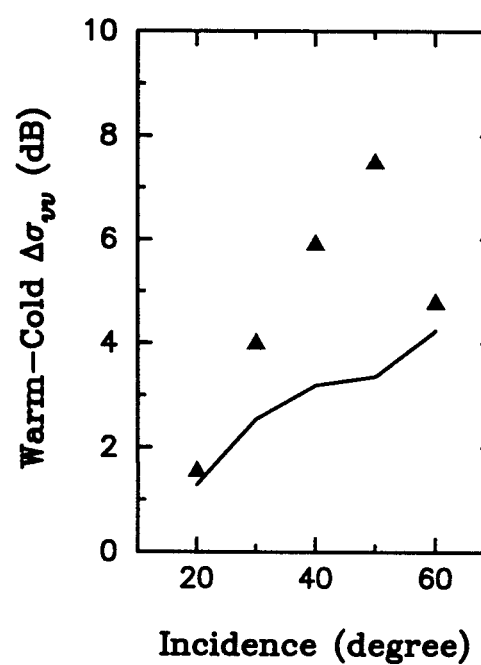
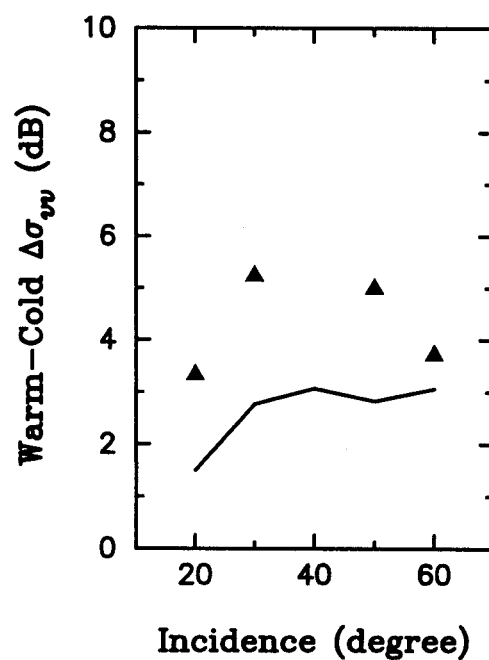
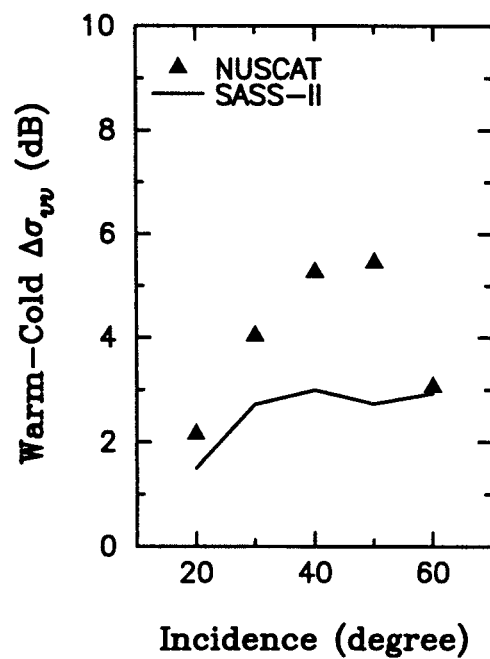
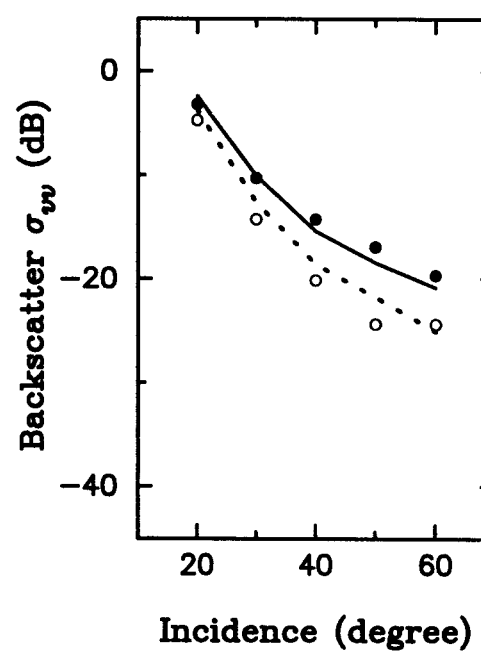
UPWIND



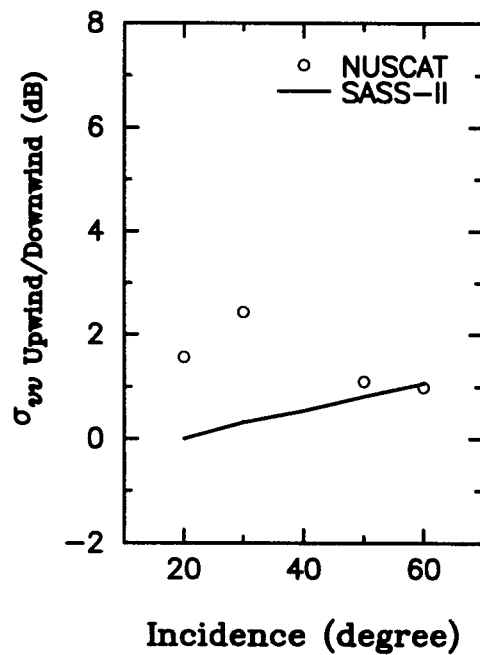
DOWNWIND



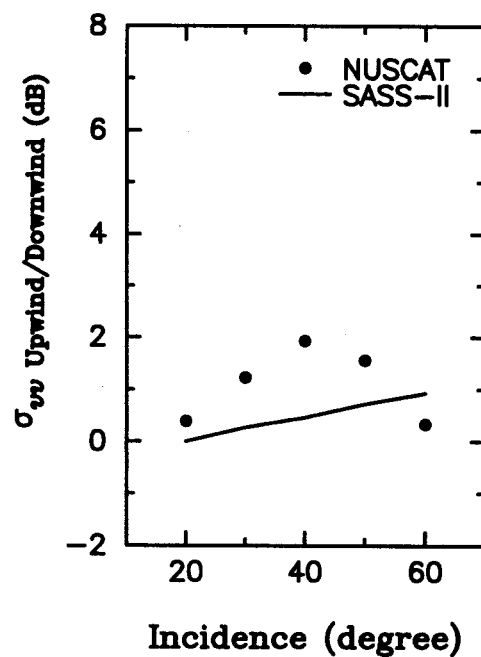
CROSSWIND



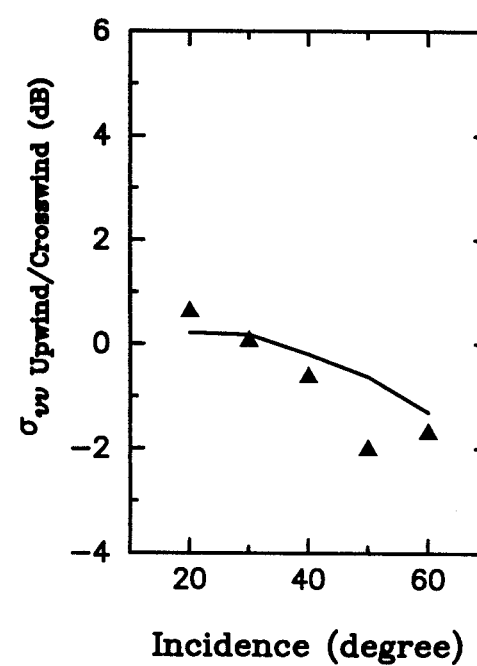
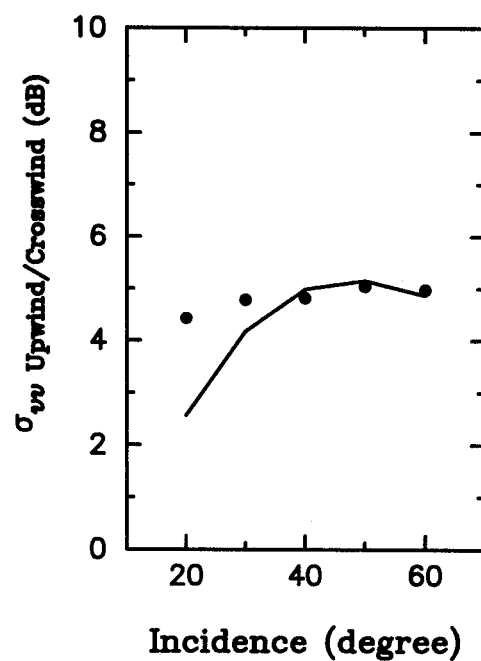
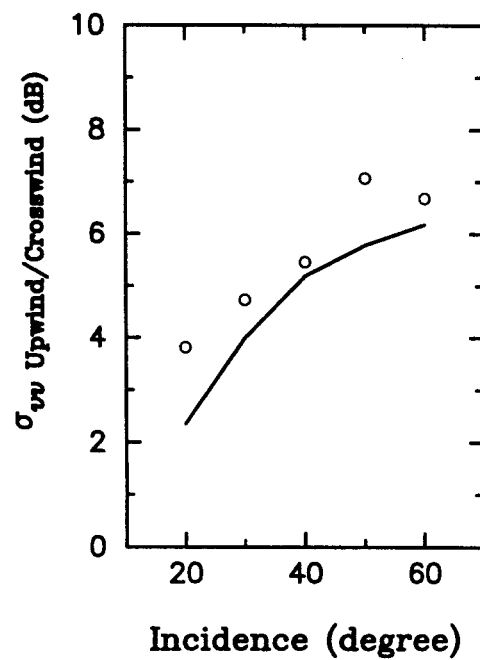
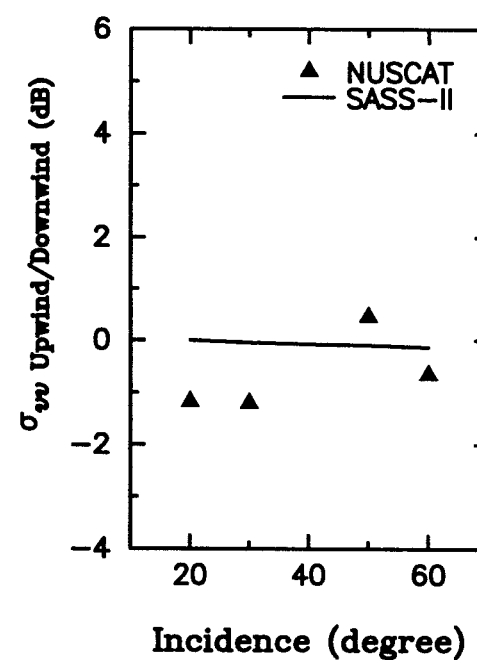
COLD SIDE

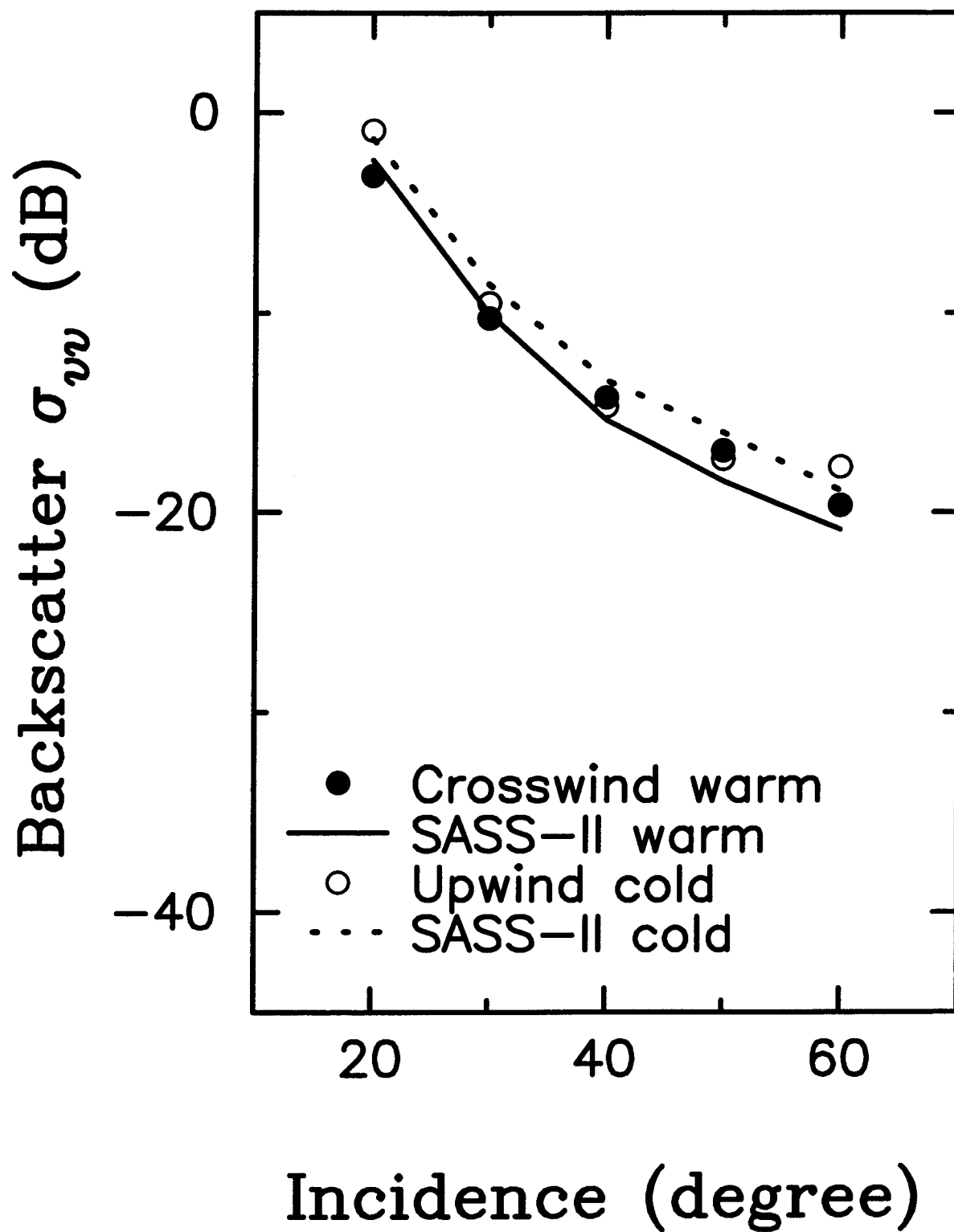


WARM SIDE



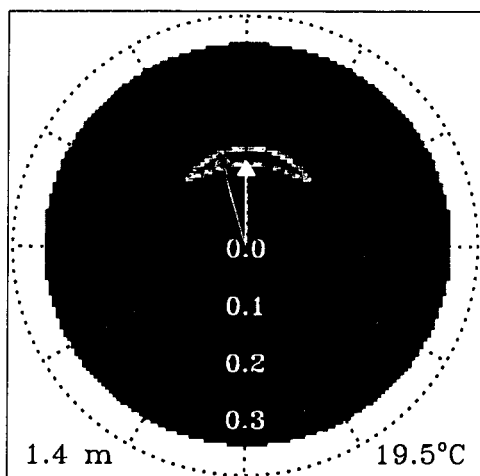
WARM-COLD



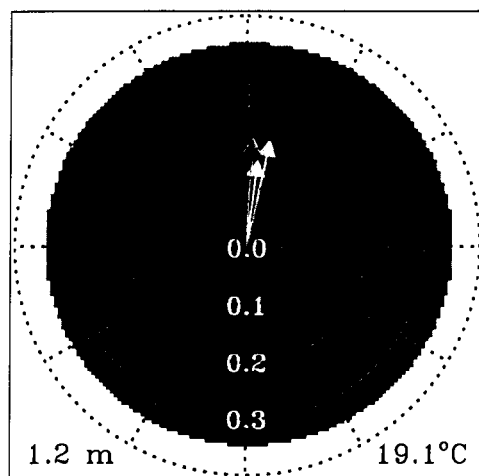




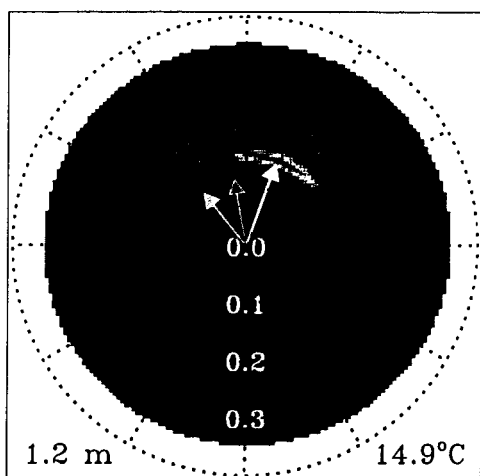
Buoy E: 91-03-09 22:00



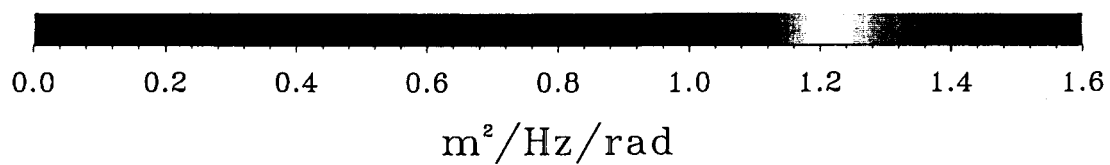
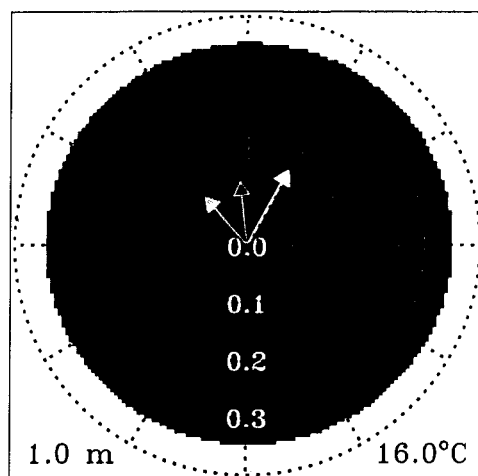
Buoy E: 91-03-10 02:00

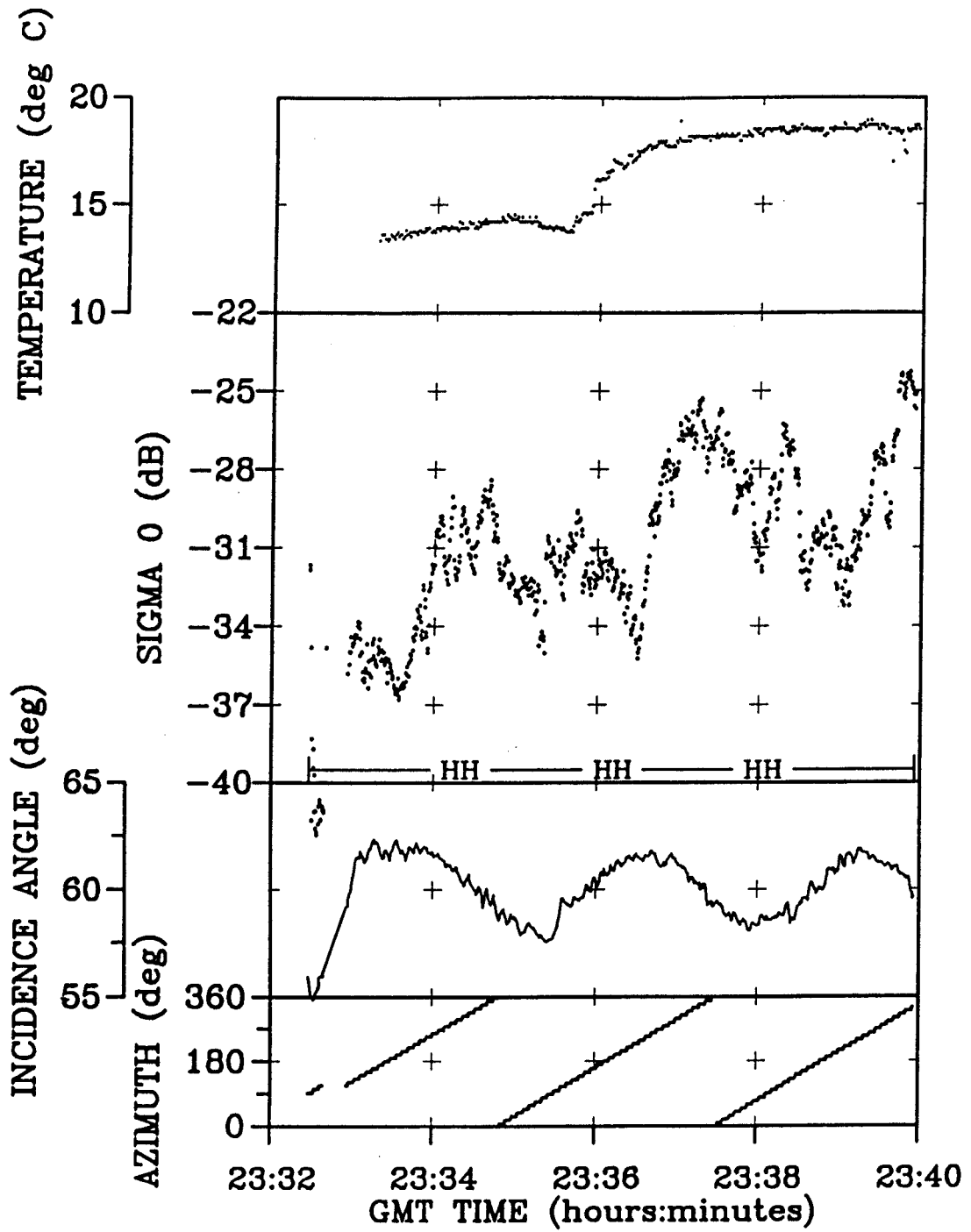


Buoy C: 91-03-09 23:00

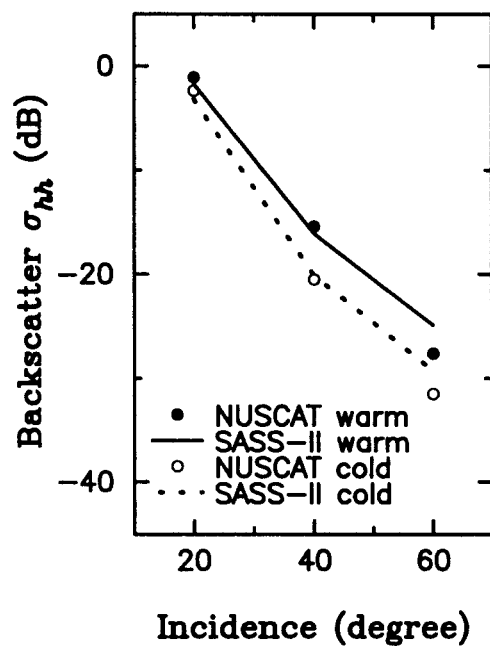


Buoy C: 91-03-10 02:00

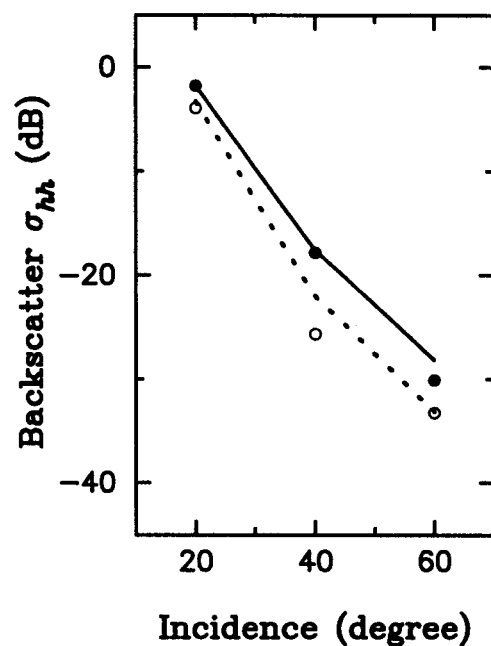




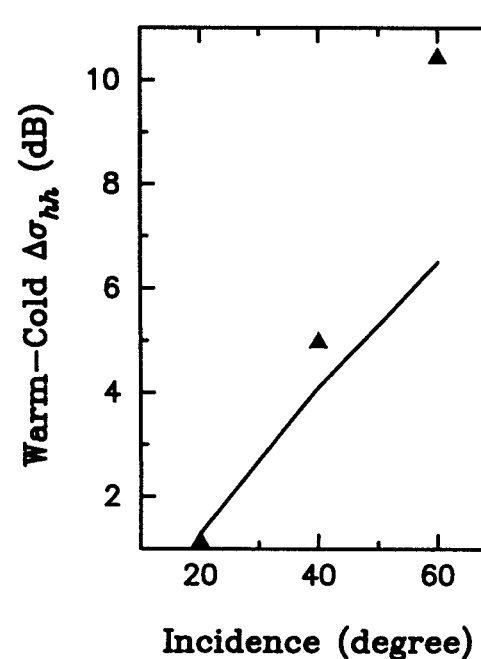
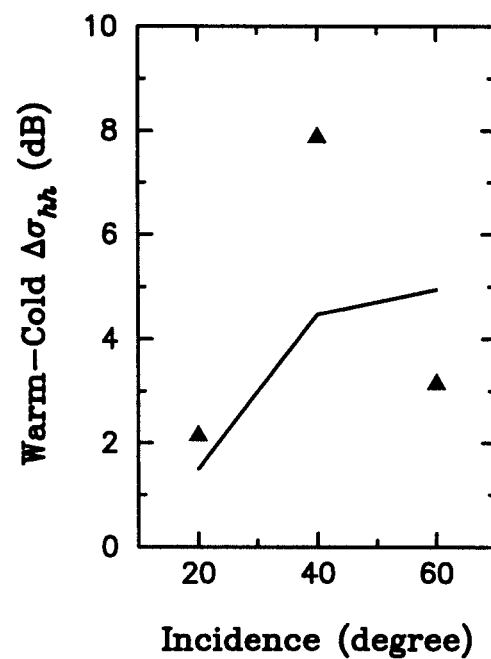
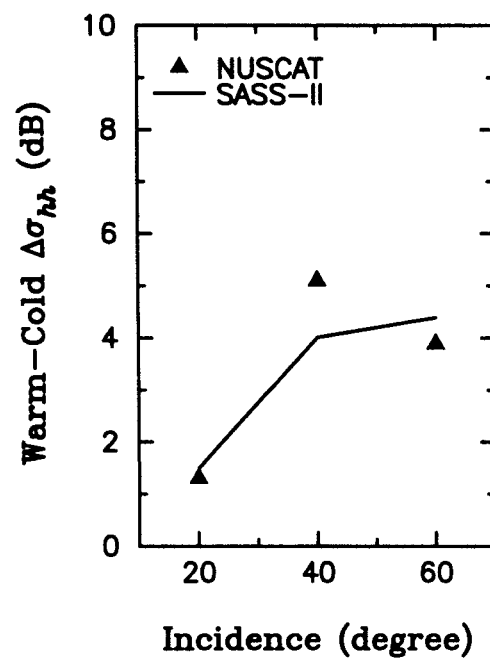
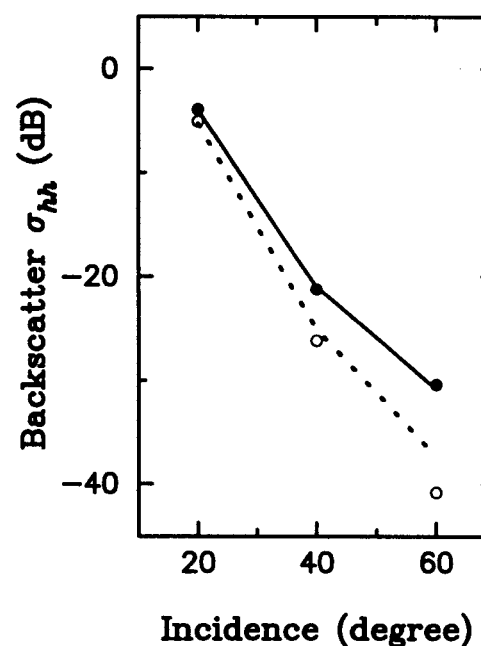
UPWIND



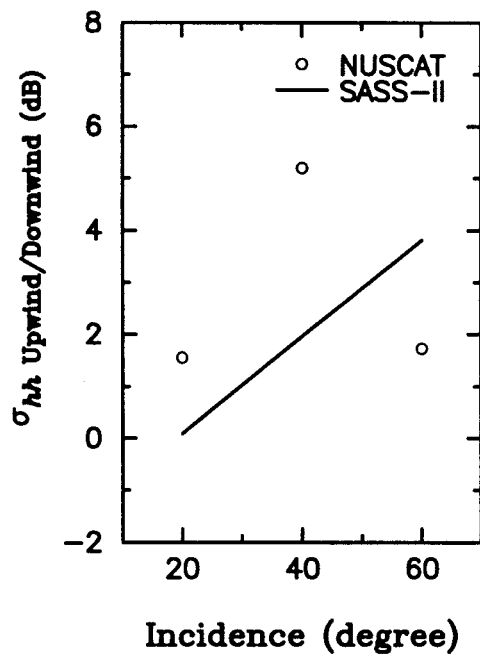
DOWNWIND



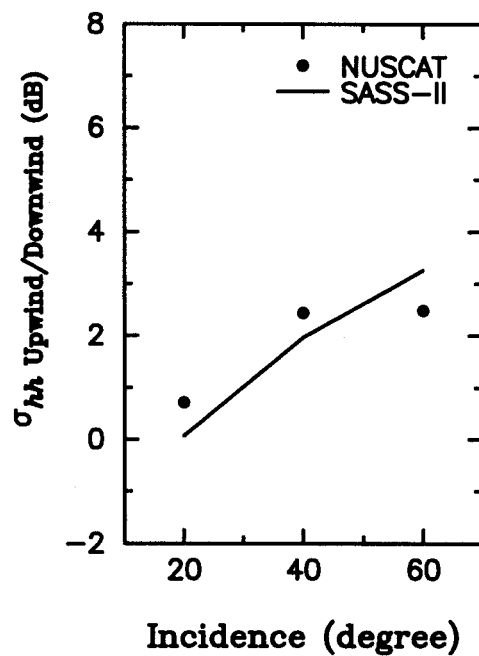
CROSSWIND



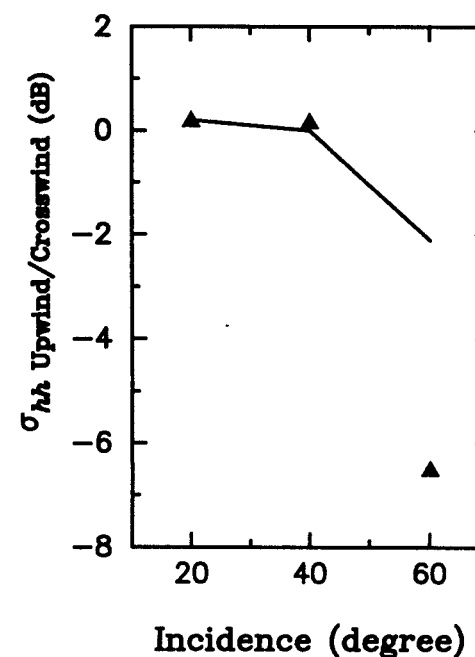
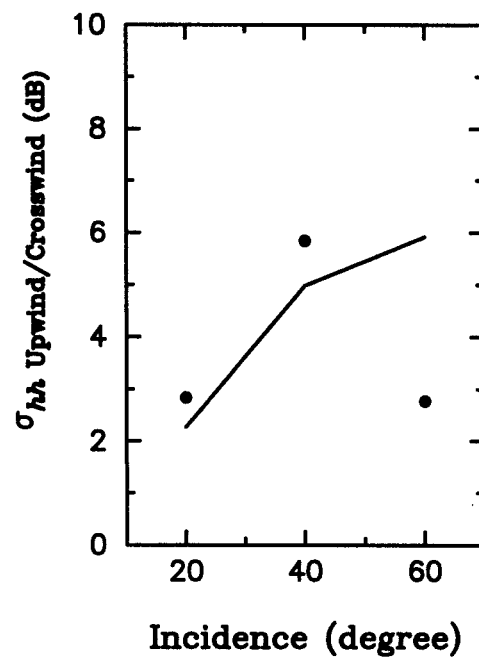
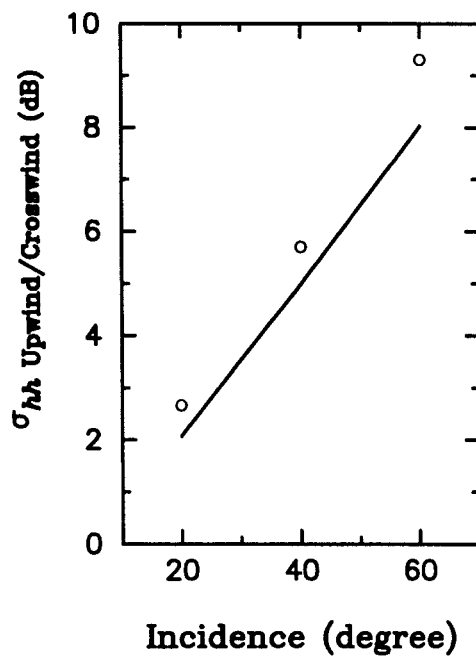
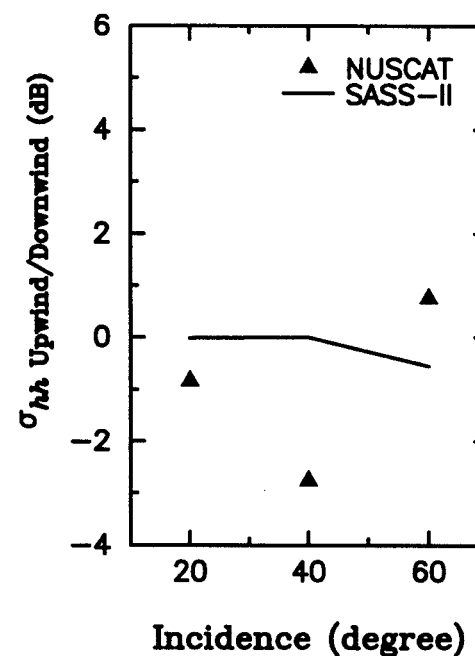
COLD SIDE

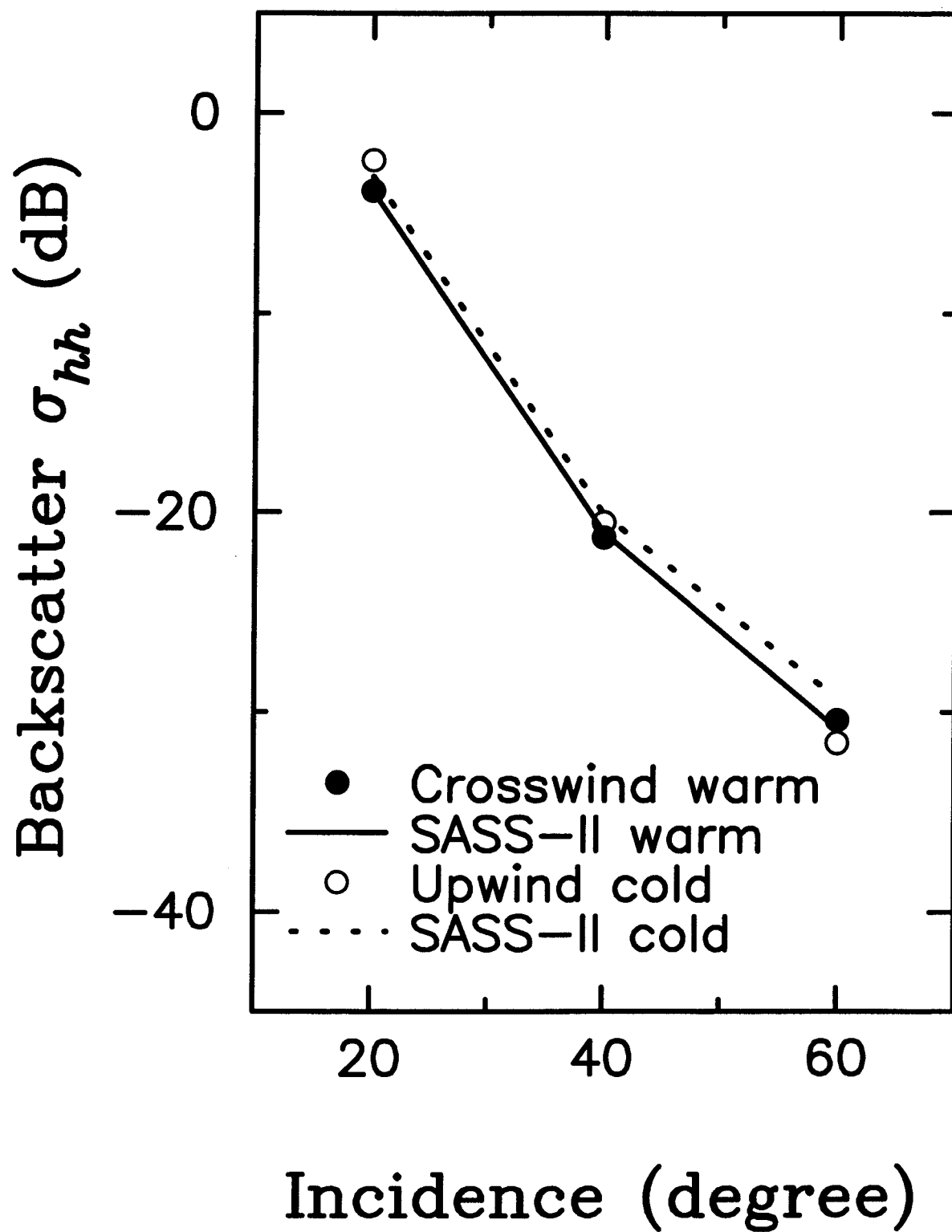


WARM SIDE



WARM-COLD





Parameter	Unit	Cold Side	Warm Side
$T_{sea}$	$^{\circ}\text{C}$	10.1/10.2	19.1/19.1
$T_{air}$	$^{\circ}\text{C}$	10.8/11.2	14.4/14.9
$Z(10)/L$	unitless	+0.003/ + 0.082	−0.148/ − 0.125
$U(\text{buoy})$	$\text{m} \cdot \text{s}^{-1}$	7.6/8.1	11.5/11.9
$U(19.5)$	$\text{m} \cdot \text{s}^{-1}$	8.5/9.1	13.5/14.0
$u_*$	$\text{m} \cdot \text{s}^{-1}$	0.27/0.29	0.46/0.48
$\phi_{wind}$	degree	205/205	214/217
$H_{1/3}$	m	1.0/1.1	1.5/1.5
$\phi_{wave}$	degree	—	187/193
$f_0$	Hz	—	0.19/0.20
$c_0/u_*$	unitless	—	13.0/17.0

**Table 1.** Atmospheric and oceanic parameters measured by buoy or derived from buoy data for the case of NUSCAT vertical polarization. Buoy A data are used for the cold side and buoy C for the warm side.

Parameter	Unit	Cold Side	Warm Side
$T_{sea}$	$^{\circ}\text{C}$	14.9/16.0	19.1/19.5
$T_{air}$	$^{\circ}\text{C}$	4.8/5.8	5.5/7.1
$Z(10)/L$	unitless	-2.08/ - 1.88	-1.13/ - 0.82
$U(\text{buoy})$	$\text{m} \cdot \text{s}^{-1}$	4.4/4.6	7.0/7.6
$U(19.5)$	$\text{m} \cdot \text{s}^{-1}$	5.6/5.8	8.6/9.2
$u_*$	$\text{m} \cdot \text{s}^{-1}$	0.18/0.19	0.28/0.30
$\phi_{wind}$	degree	319/321	12/344
$H_{1/3}$	m	1.0/1.2	1.2/1.4
$\phi_{wave}$	degree	20/29	0/7
$f_0$	Hz	0.15/0.15	0.15/0.15
$c_0/u_*$	unitless	42.0/51.4	18.1/37.6

**Table 2.** Atmospheric and oceanic parameters measured by buoy or derived from buoy data for the case of NUSCAT horizontal polarization. Buoy C data are used for the cold side and buoy E for the warm side.